Journal of Computational Physics 498 (2024) 112654

Contents lists available at ScienceDirect

Journal of Computational Physics

journal homepage: www.elsevier.com/locate/jcp

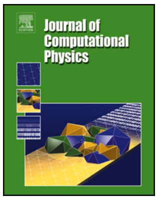

High-order adaptive multi-resolution method on curvilinear grids I: Finite difference framework

Wenhua Ma [a], Dongmi Luo [a], Shiyi Li [a], Jianxian Qiu [b], Guoxi Ni [a], Yibing Chen [a,*]

[a] *Institute of Applied Physics and Computational Mathematics, Beijing 100191, China*
[b] *School of Mathematical Sciences Xiamen University, Xiamen 361005, China*

ARTICLE INFO

Keywords:
High-order
Adaptive multi-resolution
Geometric conservation laws
WENO-ZQ scheme
Finite difference scheme

ABSTRACT

In this paper, we introduce a high-order adaptive multi-resolution method on curvilinear grids for solving hyperbolic conservation laws. To leverage the success of high-order and high-resolution schemes on Cartesian grids, the governing equations and physical variables on curvilinear grids are transformed into Cartesian grids, resulting in the introduction of additional terms related to geometric metrics. In order to achieve high-order accuracy, two techniques are employed to eliminate errors caused by geometric metrics and preserve the property of Geometric Conservation Laws (GCLs). Firstly, a newly developed and simple technique is applied to remove metric-related errors in the dissipation part of the WENO-ZQ scheme on curvilinear grids. Secondly, a GCLs-preserving data transfer operator is utilized to avoid errors caused by the metrics in the adaptive multi-resolution (MR) method on curvilinear grids. By combining these two techniques, a newly developed GCLs-preserving high-order adaptive multi-resolution method on curvilinear grids is obtained. The high-order accuracy, high resolution, and efficiency of the developed method are demonstrated through several benchmark tests conducted in one and two dimensions.

1. Introduction

Curvilinear grids are widely used in solving complex flow problems with free boundaries or complex computational domains that consist of curves. However, the methods on curvilinear grids that preserve high-order spatial accuracy and utilize adaptive mesh refinement techniques introduce new complexities and challenges even today, which remains an important issue in computational fluid dynamics.

High-order finite difference methods [12,21,22,31,40] have higher efficiency than finite volume methods [10,23,42] and discontinuous Galerkin methods [27,30], which are widely used for solving hyperbolic equations on curvilinear grids. The main idea is that the governing equations and the physical variables on curvilinear grids are transformed into Cartesian grids, and then high-order schemes are applied to solve the transformed equations. Many high-order finite difference methods have been proposed, such as the compact scheme [26], the weighted compact nonlinear scheme (WCNS) [14], the weighted essentially non-oscillatory scheme (WENO) [19,28], and the WENO-ZQ scheme [43]. The advantage of the WENO-ZQ scheme is that the associated linear weights can be any positive values as long as their sum equals one. However, the WENO-ZQ scheme hasn't been extended to curvilinear

---

* Corresponding author.
E-mail addresses: 847375670@qq.com (W. Ma), dongmiluo@stu.xmu.edu.cn (D. Luo), lishiyi14@tsinghua.org.cn (S. Li), jxqiu@xmu.edu.cn (J. Qiu), gxni@iapcm.ac.cn (G. Ni), chen_yibing@iapcm.ac.cn (Y. Chen).

https://doi.org/10.1016/j.jcp.2023.112654
Received 8 December 2022; Received in revised form 12 August 2023; Accepted 18 November 2023

grids. For high-order finite difference methods on curvilinear grids, geometric conservation laws (GCLs) are a significant property. Although, the metrics from transformation analytically satisfy GCLs known as the freestream preservation, some discretized forms of metrics and high-order schemes violate the GCLs. If the GCLs property is not satisfied, the metrics in these schemes may introduce numerical errors from the freestream and cause oscillations, and sometimes result in numerical instability [32]. To preserve the GCLs property on curvilinear grids, Deng et al. [13] presented the symmetrical conservative metric method (SCMM) for the WCNS scheme by incorporating the independent interpolation of flow variables and spatial metrics. Moreover, splitting the WENO flux into a central component and a dissipation component is another way to maintain the GCLs property. The main idea is to eliminate the error caused by the metrics of the coordinate transformation. Nonomura et al. [31] modified the origin finite difference WENO scheme by freezing metrics and Jacobian for the entire stencil to cancel the dissipation component. Vinokur and Yee [39] disregarded the influence of the grid Jacobian and replaced the transformed conservative variables with the original variables of the dissipation term. And Zhu and Hu [45] presented a hybrid-WENO scheme which modified the dissipation term by sharing the same metrics. Different from techniques mentioned above, in this paper, we proposed a GCLs-preserving WENO-ZQ scheme by splitting technique above and reformulating the dissipation component into a local difference form and modifying it into a GCLs-preserving form.

High-order spatial accuracy doesn't mean high resolution. To resolve fine scale structures and smooth flow features and therefore obtain high resolution flow fields with as little computational demand as possible, adaptive techniques are required.

The h-adaptive method has the advantage of not requiring solving extra PDEs and having less dependence on the initial grid, which is widely used. Both the adaptive mesh refinement (AMR) method [3,8,11,29] and the adaptive multi-resolution (MR) method [5,15–18] are h-adaptive methods that have been well-developed in recent years. The adaptive mesh refinement method (AMR) was originally designed by Berger and Colella [4], whose grid adaptation is made by estimating the local discretization errors in space. Harten [17] first introduced the adaptive multi-resolution method (MR) as a strategy for spatial adaptivity. The MR method employs a wavelet-based representation of the flow fields to reduce the data to the bare minimum. Domingues et al. [15] developed an adaptive MR method with local time stepping to solve the conservation laws. Han et al. [16] coupled the adaptive MR method and a sharp interface model to simulate multi-phase flows. As mentioned in [11], MR methods offer greater computational efficiency and memory compression rate than AMR methods in two space dimensions.

Coupling high-order finite-difference schemes and h-adaptive methods on curvilinear grids can be problematic. If the data transfer in h-adaptive methods don't satisfy the GCLs property, errors caused by evaluation of the Jacobian and metrics can cause oscillations, degrade the accuracy, and even result in instability. Chen et al. [8] proposed a fifth-order accurate finite difference method coupled with the adaptive mesh refinement (AMR) method on curvilinear grids. And, this method necessitates additional operators when resolution changes, meaning that different interpolation polynomials need to be constructed for different adaptive grid cases. In this paper, we focus on the adaptive MR method. However, in the literature, the adaptive MR method hasn't been extended to curvilinear grids, and the coupling of a high-order finite difference scheme with the adaptive MR method on curvilinear grids has not been found yet.

In this paper, we proposed a high-order adaptive multi-resolution method on curvilinear grids. The method has three primary components. First, the governing equations and physical variables on curvilinear grids are transformed into Cartesian grids, which contain the geometric metrics. Second, to achieve the designed high-order accuracy, a new fifth-order GCLs-preserving WENO-ZQ scheme is proposed to solve the transformed governing equations. Finally, to further improve the resolution near discontinuities, the adaptive multi-resolution method is also extended to curvilinear grids. To reduce the error caused by the geometric metrics of the coordinate transformation, the data transfer operators, such as the prediction and projection operators are reformulated. Coupling the GCLs-preserving WENO-ZQ scheme and the adaptive multi-resolution method, we obtained the new high-order adaptive multi-resolution method on curvilinear grids. The proposed method avoids the complexity of directly constructing a high-order adaptive method on curvilinear grids by using coordination transformations and careful management of geometric metrics. Several benchmark tests in one and two spatial dimensions are used to demonstrate the high-order accuracy and efficiency of the developed method.

This paper is organized as follows: In section 2, the governing equations in Cartesian and curvilinear grids and the equation of states are described. The fifth-order GCLs-preserving WENO-ZQ scheme is proposed to compute the numerical fluxes, spatial metrics and Jacobian. In section 3, the Cartesian adaptive multi-resolution method is extended to implementation on curvilinear grids, including the transformed projection and prediction operators. The block-based data structure and local time stepping algorithm are also introduced to improve the efficiency and reduce computation costs. Numerical tests are presented in Section 4.

2. High-order finite difference scheme on curvilinear grids

2.1. Governing equation

In this subsection, we considered two-dimensional hyperbolic systems, such as Euler equations on Cartesian grids (t, x, y),

$$\mathbf{U}_t + \mathbf{F}(\mathbf{U})_x + \mathbf{G}(\mathbf{U})_y = \mathbf{0}. \tag{1}$$

where ρ, u, v, E denote the density, and the velocity components in the $x-, y-$directions, and total energy, respectively. The conservative variables are represented by $\mathbf{U} = (\rho, \rho u, \rho v, E)^T$, and the numerical fluxes are given by $\mathbf{F}(\mathbf{U}) = \left(\rho u, \rho u^2 + p, \rho uv, (E+p)u\right)^T$, $\mathbf{G}(\mathbf{U}) = \left(\rho u, \rho uv, \rho v^2 + p, (E+p)v\right)^T$.

The total energy is

$$E = \rho e + \frac{1}{2}\rho(u^2 + v^2), \tag{2}$$

where e is the specific internal energy.

To develop a numerical scheme in curvilinear coordinates, we consider the coordinate transformation from the physical domain (x, y) to the computational domain (ξ, η), incorporating Jacobian and metrics,

$$J = \left(\frac{\partial(x,y)}{\partial(\xi,\eta)}\right) = \begin{pmatrix} x_\xi & x_\eta \\ y_\xi & y_\eta \end{pmatrix}. \tag{3}$$

With the transformation above, the two-dimensional Euler equations on curvilinear grids (t, ξ, η) are expressed as

$$\widetilde{\mathbf{U}}_t + \widetilde{\mathbf{F}}(\widetilde{\mathbf{U}})_\xi + \widetilde{\mathbf{G}}(\widetilde{\mathbf{U}})_\eta = \mathbf{0}, \tag{4}$$

where the conservative variables are $\widetilde{\mathbf{U}} = J\mathbf{U}$. The numerical fluxes are $\widetilde{\mathbf{F}} = J(\xi_x \mathbf{F} + \xi_y \mathbf{G})$ and $\widetilde{\mathbf{G}} = J(\eta_x \mathbf{F} + \eta_y \mathbf{G})$. The details for $\widetilde{\mathbf{U}}$ and $\widetilde{\mathbf{F}}, \widetilde{\mathbf{G}}$ are

$$\widetilde{\mathbf{U}} = J\begin{pmatrix} \rho \\ \rho u \\ \rho v \\ E \end{pmatrix}, \quad \widetilde{\mathbf{F}} = J\begin{pmatrix} \rho U \\ \rho u U + \xi_x p \\ \rho v U + \xi_y p \\ (E+p)U \end{pmatrix}, \quad \widetilde{\mathbf{G}} = J\begin{pmatrix} \rho V \\ \rho u V + \eta_x p \\ \rho v V + \eta_y p \\ (E+p)V \end{pmatrix}, \tag{5}$$

where $U = u\xi_x + v\xi_y$ and $V = u\eta_x + v\eta_y$. The Jacobian J and metrics $\xi_x, \xi_y, \eta_x, \eta_y$ are expressed as

$$\begin{aligned} J &= \left|\frac{\partial(x,y)}{\partial(\xi,\eta)}\right| = x_\xi y_\eta - x_\eta y_\xi, \\ \xi_x &= \frac{1}{J} y_\eta, \qquad \xi_y = -\frac{1}{J} x_\eta, \\ \eta_x &= -\frac{1}{J} y_\xi, \quad \eta_y = \frac{1}{J} x_\xi. \end{aligned}$$

In a uniform flow field, the numerical fluxes $\mathbf{F}$ and $\mathbf{G}$ become constant values. As a result, the transformed equations can be simplified as

$$\begin{aligned} (J\xi_x)_\xi + (J\eta_x)_\eta &= 0, \\ (J\xi_y)_\xi + (J\eta_y)_\eta &= 0, \end{aligned}$$

which is called the geometric conservation laws (GCLs). Researches [12,31,40,45] show that for high-order finite difference schemes being applied on curvilinear grids, the violation of GCLs might cause large errors and even result in numerical instability. As stated in [31], the standard finite-difference WENO scheme and fluxes cannot maintain GCLs. Deng et al. [12] and Abe et al. [1] have extensively discussed the GCLs and the calculation of metrics, and have provided the symmetrical conservative metric method for calculating the metrics for the GCLs. All metrics must be rewritten into conservative form and evaluated in the same way.

For simplicity, the system is closed by the ideal gas equation of state (EOS):

$$p = (\gamma - 1)\rho e, \tag{6}$$

where γ is the specific heat ratio.

2.2. Discretization scheme on two-dimensional curvilinear grids

In the computational domain, we consider the semi-discretized finite difference scheme in the cell (i, j) as

$$\frac{d\widetilde{\mathbf{U}}_{i,j}}{dt} = \mathcal{L}(\widetilde{\mathbf{U}}_{i,j}) = -\frac{1}{\Delta\xi}\left(\widetilde{\mathbf{F}}_{i+1/2,j} - \widetilde{\mathbf{F}}_{i-1/2,j}\right) - \frac{1}{\Delta\eta}\left(\widetilde{\mathbf{G}}_{i,j+1/2} - \widetilde{\mathbf{G}}_{i,j-1/2}\right), \tag{7}$$

where $\widetilde{\mathbf{U}}_{i,j}$ is the point value at the cell (i, j) center. And $\widetilde{\mathbf{F}}_{i+1/2,j}$ is the numerical flux in the computational domain. $\Delta\xi$ and $\Delta\eta$ are cell sizes in ξ- and η-direction, respectively.

To achieve high-order spatial accuracy, the fifth-order WENO-ZQ reconstruction [43] is adopted. Since the computational domain is equidistant and Cartesian, the fluxes can be arranged dimension by dimension. The stencil for reconstructing the flux at $\xi = \xi_{i+1/2}$ is $\left\{\xi_{i-2}, \xi_{i-1}, \xi_i, \xi_{i+1}, \xi_{i+2}\right\}$. The four steps for updating the point value $\widetilde{\mathbf{U}}_{i,j}$ are as follows.

Step 1. The ξ-direction cell-centered flux $\widetilde{\mathbf{F}}_{i,j}$ is calculated by $\widetilde{\mathbf{F}}_{i,j} = (y_\eta)_{i,j}\mathbf{F}_{i,j} + (-x_\eta)_{i,j}\mathbf{G}_{i,j}$. Similarly, the η-direction cell-centered flux $\widetilde{\mathbf{G}}_{i,j}$ is calculated by $\widetilde{\mathbf{G}}_{i,j} = (-y_\xi)_{i,j}\mathbf{F}_{i,j} + (x_\xi)_{i,j}\mathbf{G}_{i,j}$. Here, $\mathbf{F}_{i,j}$ and $\mathbf{G}_{i,j}$ are the cell-centered fluxes in the physical domain.

Step 2. The cell-centered fluxes and conservative variables within the stencil are transformed into characteristic space, and then the local Lax-Friedrichs splitting is applied.

Step 3. Within the stencil, a fifth-order WENO-ZQ scheme is applied to reconstruct characteristic fluxes at the half point, which are transformed back into the computational space to obtain the numerical flux $\widetilde{\mathbf{F}}_{i+1/2,j}$ at $\xi = \xi_{i+1/2}$.

Step 4. After all the reconstructed fluxes are obtained, the point value $\widetilde{\mathbf{U}}_{i,j}$ at the center of the cell (i, j) can be evolved via scheme (7) with a TVD Runge-Kutta scheme.

2.3. Fifth-order GCLs-preserving WENO-ZQ scheme

Firstly, the standard fifth-order WENO-ZQ scheme on Cartesian grids is briefly introduced as follows. Then, the fifth-order GCLs-preserving WENO-ZQ scheme is introduced on curvilinear grids.

2.3.1. The standard fifth-order WENO-ZQ scheme on Cartesian grids

In the beginning, numerical fluxes and conservative variables within the stencil are transformed into characteristic space. Then, the local Lax-Friedrichs splitting method is applied.

$$\mathbf{f}_k^{\pm} = \frac{1}{2}\mathbf{L}_{i+1/2}\left(\widetilde{\mathbf{F}}_k \pm \lambda \widetilde{\mathbf{U}}_k\right), k = i-2, i-1, ..., i+2, i+3, \tag{8}$$

where $\mathbf{f}_k^{\pm}$ represents the characteristic flux, $\mathbf{L}_{i+1/2}$ denotes the left eigenvector matrix of the linearized Roe-average Jacobian matrix and $\lambda = \max(|\lambda_k|)$ is the largest eigenvalue of the linearized Roe-average Jacobian matrix within the stencil.

We take one component f_k^+ in the positive characteristic fluxes $\mathbf{f}_k^+$ as an example. The positive numerical fluxes f_k^+ that approximate the reconstructed numerical fluxes $f_{i+1/2}^+$ are reconstructed in four steps.

Step 1. Choose one big stencil $T_1 = \{\xi_{i-2}, \xi_{i-1}, \xi_i, \xi_{i+1}, \xi_{i+2}\}$ and two small stencils $T_2 = \{\xi_{i-1}, \xi_i\}$, $T_3 = \{\xi_i, \xi_{i+1}\}$, and then construct a quadratic polynomial $p_1^+(\xi)$ and two linear polynomials $p_2^+(\xi), p_3^+(\xi)$ respectively which are satisfying:

$$\begin{aligned}
&\frac{1}{h}\int_{\xi_k-h/2}^{\xi_k+h/2} p_1(\xi)d\xi = f_k^+, k = i-2, i-1, i, i+1, i+2,\\
&\frac{1}{h}\int_{\xi_k-h/2}^{\xi_k+h/2} p_2(\xi)d\xi = f_k^+, k = i-1, i,\\
&\frac{1}{h}\int_{\xi_k-h/2}^{\xi_k+h/2} p_3(\xi)d\xi = f_k^+, k = i, i+1,
\end{aligned} \tag{9}$$

where $h = \xi_{i+1/2} - \xi_{i-1/2}$ is the uniform cell size in the computational domain.

Step 2. Rewrite $p_1^+(\xi)$ as

$$p_1^+(\xi) = \gamma_1\left(\frac{1}{\gamma_1}p_1^+(\xi) - \frac{\gamma_2}{\gamma_1}p_2^+(\xi) - \frac{\gamma_3}{\gamma_1}p_3^+(\xi)\right) + \gamma_2 p_2^+(\xi) + \gamma_3 p_3^+(\xi).$$

Here, the associated linear weights $\gamma_1, \gamma_2, \gamma_3$ can be any positive values as long as the condition $\gamma_1 + \gamma_2 + \gamma_3 = 1$ is satisfied. We choose the linear weights $\gamma_1 = 0.98$, $\gamma_2 = \gamma_3 = 0.01$ which satisfy $\gamma_1 + \gamma_2 + \gamma_3 = 1$.

Step 3. The non-linear weights are obtained based on the associated linear weights and the smoothness indicators,

$$\omega_k^+ = \frac{\hat{\omega}_k}{\sum_{kk=1}^{3}\hat{\omega}_{kk}}, \quad \hat{\omega}_k = \gamma_k\left(1 + \frac{\tau}{(\beta_k^+ + \epsilon)^2}\right), \quad k = 1, 2, 3, \tag{10}$$

where ϵ is a small positive number to avoid the denominator becoming zero, which is $\epsilon = 10^{-6}$ in all tests. τ denotes the absolute deference between β_k, which is defined as

$$\tau = \left(\frac{|\beta_1^+ - \beta_2^+| + |\beta_1^+ - \beta_3^+|}{2}\right)^2.$$

The smoothness indicators β_k^+ are calculated as specified in [37].

$$\begin{aligned}
\beta_1^+ = {} & \frac{1}{144}\left(f_{i-2}^+ - 8f_{i-1}^+ + 8f_{i+1}^+ - f_{i+2}^+\right)^2\\
& + \frac{1}{15600}\left(-11f_{i-2}^+ + 174f_{i-1}^+ - 326f_i^+ + 174f_{i+1}^+ - 11f_{i+2}^+\right)^2\\
& + \frac{781}{2880}\left(-f_{i-2}^+ + 2f_{i-1}^+ - 2f_{i+1}^+ + f_{i+2}^+\right)^2\\
& + \frac{1421461}{1310400}\left(f_{i-2}^+ - 4f_{i-1}^+ + 6f_i^+ - 4f_{i+1}^+ + f_{i+2}^+\right)^2,\\
\beta_2^+ = {} & \left(f_{i-1}^+ - f_i^+\right)^2,\\
\beta_3^+ = {} & \left(f_i^+ - f_{i+1}^+\right)^2.
\end{aligned}$$

Step 4. The final reconstruction of numerical fluxes $f^+(\xi)$ at the point $\xi_{i+\frac{1}{2}}$ in the target cell I_i is given by

$$f^+_{i+\frac{1}{2}} = \omega^+_1 \left(\frac{1}{\gamma_1} p^+_1(\xi_{i+\frac{1}{2}}) - \frac{\gamma_2}{\gamma_1} p^+_2(\xi_{i+\frac{1}{2}}) - \frac{\gamma_3}{\gamma_1} p^+_3(\xi_{i+\frac{1}{2}}) \right) + \omega^+_2 p^+_2(\xi_{i+\frac{1}{2}}) + \omega^+_3 p^+_3(\xi_{i+\frac{1}{2}}). \tag{11}$$

Here, polynomials $p^+_1(\xi_{i+\frac{1}{2}}), p^+_2(\xi_{i+\frac{1}{2}}), p^+_3(\xi_{i+\frac{1}{2}})$ are

$$\begin{aligned}
p^+_1(\xi_{i+\frac{1}{2}}) &= \frac{1}{60}\left(2f^+_{i-2} - 13f^+_{i-1} + 47f^+_i + 27f^+_{i+1} - 3f^+_{i+2}\right),\\
p^+_2(\xi_{i+\frac{1}{2}}) &= \frac{1}{60}\left(90f^+_i - 30f^+_{i-1}\right),\\
p^+_3(\xi_{i+\frac{1}{2}}) &= \frac{1}{60}\left(30f^+_i + 30f^+_{i+1}\right).
\end{aligned}$$

Note that, the negative fluxes $f^-_{i+\frac{1}{2}}$ can be obtained by flipping the stencils, similarly. The numerical fluxes at $\xi = \xi_{i+\frac{1}{2}}$ can be calculated by transforming the characteristic fluxes back into computational space as

$$\widetilde{\mathbf{F}}_{i+\frac{1}{2}} = \mathbf{R}_{i+\frac{1}{2}} \left(\mathbf{f}^+_{i+\frac{1}{2}} + \mathbf{f}^-_{i+\frac{1}{2}} \right).$$

2.3.2. The fifth-order GCLs-preserving WENO-ZQ scheme on curvilinear grids

As indicated by Nonomura et al. [31,32], the standard WENO scheme cannot preserve GCLs due to two reasons. Firstly, the metrics cannot be evaluated through upwinding schemes, rendering it impossible to use conservative metrics techniques [13]. Secondly, when the freestream is imposed, oscillating spatial metrics cause non-ideal weights. This is also the reason why the WENO-ZQ scheme fails to maintain GCLs. The method proposed in this paper resolves both of these problems and enables the WENO-ZQ scheme to maintain GCLs on curvilinear grids. The WENO-ZQ fluxes can be divided into a central component and a dissipation component, as in Jiang and Wu [20],

$$\begin{aligned}
\widetilde{\mathbf{F}}_{i+\frac{1}{2}} &= \widetilde{\mathbf{F}}^+_{i+\frac{1}{2}} + \widetilde{\mathbf{F}}^-_{i+\frac{1}{2}}\\
&= \frac{1}{60}\left(\widetilde{\mathbf{F}}_{i-2} - 8\widetilde{\mathbf{F}}_{i-1} + 37\widetilde{\mathbf{F}}_i + 37\widetilde{\mathbf{F}}_{i+1} - 8\widetilde{\mathbf{F}}_{i+2} + \widetilde{\mathbf{F}}_{i+3}\right)\\
&- \frac{1}{60}\sum_m \mathbf{R}_m \left\{ \left(\hat{\omega}^+_2 + \hat{\omega}^+_3 - 1\right)\hat{f}^+_1 + (\hat{\omega}^+_2 + \hat{\omega}^+_3)\hat{f}^+_2 - 30\hat{\omega}^+_3 \hat{f}^+_3 - (\hat{\omega}^+_2 + \hat{\omega}^+_3)\hat{f}^+_4 \right\}\\
&+ \frac{1}{60}\sum_m \mathbf{R}_m \left\{ \left(\hat{\omega}^-_2 + \hat{\omega}^-_3 - 1\right)\hat{f}^-_1 + (\hat{\omega}^-_2 + \hat{\omega}^-_3)\hat{f}^-_2 - 30\hat{\omega}^-_3 \hat{f}^-_3 - (\hat{\omega}^-_2 + \hat{\omega}^-_3)\hat{f}^-_4 \right\},
\end{aligned} \tag{12}$$

where

$$\begin{aligned}
&\hat{f}^+_1 = \mathbf{f}^+_{i-2} - 5\mathbf{f}^+_{i-1} + 10\mathbf{f}^+_i - 10\mathbf{f}^+_{i+1} + 5\mathbf{f}^+_{i+2} - \mathbf{f}^+_{i+3},\\
&\hat{f}^+_2 = \mathbf{f}^+_{i-2} - 8\mathbf{f}^+_{i-1} + 37\mathbf{f}^+_i - 37\mathbf{f}^+_{i+1} + 8\mathbf{f}^+_{i+2} - \mathbf{f}^+_{i+3},\\
&\hat{f}^+_3 = \mathbf{f}^+_{i+1} - 2\mathbf{f}^+_i + \mathbf{f}^+_{i-1},\ \hat{f}^+_4 = 16\mathbf{f}^+_i - 14\mathbf{f}^+_{i-1} - 2\mathbf{f}^+_{i-2},\\
&\hat{f}^-_1 = \mathbf{f}^-_{i-2} - 5\mathbf{f}^-_{i-1} + 10\mathbf{f}^-_i - 10\mathbf{f}^-_{i+1} + 5\mathbf{f}^-_{i+2} - \mathbf{f}^-_{i+3},\\
&\hat{f}^-_2 = \mathbf{f}^-_{i-2} - 8\mathbf{f}^-_{i-1} + 37\mathbf{f}^-_i - 37\mathbf{f}^-_{i+1} + 8\mathbf{f}^-_{i+2} - \mathbf{f}^-_{i+3},\\
&\hat{f}^-_3 = \mathbf{f}^-_i - 2\mathbf{f}^-_{i+1} + \mathbf{f}^-_{i+2},\ \hat{f}^-_4 = 16\mathbf{f}^-_{i+1} - 14\mathbf{f}^-_{i+2} - 2\mathbf{f}^-_{i+3}.
\end{aligned} \tag{13}$$

And positive non-linear weights $\hat{\omega}^+_l, l = 1,2,3$ in Eq. (12) satisfy $\hat{\omega}^+_1 = \frac{\omega^+_1}{\gamma_1}, \hat{\omega}^+_2 = (\omega^+_2 - \omega^+_1 \frac{\gamma_2}{\gamma_1}), \hat{\omega}^+_3 = (\omega^+_3 - \omega^+_1 \frac{\gamma_3}{\gamma_1})$. Non-linear weights $\omega^+_l, l = 1,2,3$ are obtained by Eq. (10) for positive fluxes. Negative non-linear weights $\hat{\omega}^-_l, l = 1,2,3$ are obtained similarly.

To preserve the GCLs property, on one hand, in Eq. (12), for the central component, the symmetrical conservative metric method can be applied. The error caused by metrics vanishes if the central component and metrics are evaluated by the same scheme for each direction. Jacobians and metrics at half-point are calculated by a sixth-order central scheme as the central component. Here, we take $(J)_{i+\frac{1}{2}}$ as an example,

$$(J)_{i+\frac{1}{2}} = \frac{1}{60}\left[(J)_{i-2} - 8(J)_{i-2} + 37(J)_i + 37(J)_{i+1} - 8(J)_{i+2} + (J)_{i+3}\right]. \tag{14}$$

On the other hand, when freestream is imposed, the dissipation component is not zero due the existent of the metrics in Eq. (13). In order to eliminate the dissipation component, Nonomura et al. [32] used the method of freezing Jacobian and metric terms at half-point. Vinokur and Yee [39] disregarded the influence of the grid Jacobian and replaced the transformed conservative variables with the original variables. Different from these methods, in this paper, we rewrite the dissipation component into a local difference form and reformulate it to preserve the GCLs property. We take the first term $\hat{f}_1^+$ in Eq. (13) as an example.

$$\begin{aligned}\hat{f}_1^+ &= \mathbf{f}_{i-2}^+ - 5\mathbf{f}_{i-1}^+ + 10\mathbf{f}_i^+ - 10\mathbf{f}_{i+1}^+ + 5\mathbf{f}_{i+2}^+ - \mathbf{f}_{i+3}^+ \\ &= \frac{1}{2}\mathbf{L}_{i+\frac{1}{2}} \cdot \left[\left(\widetilde{\mathbf{F}}_{i-2} - \widetilde{\mathbf{F}}_{i-1}\right) - 4\left(\widetilde{\mathbf{F}}_{i-1} - \widetilde{\mathbf{F}}_i\right) + 6\left(\widetilde{\mathbf{F}}_i - \widetilde{\mathbf{F}}_{i+1}\right) - 4\left(\widetilde{\mathbf{F}}_{i+1} - \widetilde{\mathbf{F}}_{i+2}\right) + \left(\widetilde{\mathbf{F}}_{i+2} - \widetilde{\mathbf{F}}_{i+3}\right)\right] \\ &+ \frac{1}{2}\lambda\mathbf{L}_{i+\frac{1}{2}} \cdot \left[\left(\widetilde{\mathbf{U}}_{i-2} - \widetilde{\mathbf{U}}_{i-1}\right) - 4\left(\widetilde{\mathbf{U}}_{i-1} - \widetilde{\mathbf{U}}_i\right) + 6\left(\widetilde{\mathbf{U}}_i - \widetilde{\mathbf{U}}_{i+1}\right) - 4\left(\widetilde{\mathbf{U}}_{i+1} - \widetilde{\mathbf{U}}_{i+2}\right) + \left(\widetilde{\mathbf{U}}_{i+2} - \widetilde{\mathbf{U}}_{i+3}\right)\right].\end{aligned} \tag{15}$$

Then, by substituting $\widetilde{\mathbf{F}} = J(\xi_x\mathbf{F} + \xi_y\mathbf{G})$ into Eq. (15), we can modify Eq. (15) into a GCLs-preserving form, which is as

$$\begin{aligned}\hat{f}_1^+ = \frac{1}{2}\mathbf{L}_{i+\frac{1}{2}} \cdot &\Big[\left(\mathbf{F}_{i-2} - \mathbf{F}_{i-1}\right)\left(J\xi_x\right)_{i-\frac{3}{2}} - 4\left(\mathbf{F}_{i-1} - \mathbf{F}_i\right)\left(J\xi_x\right)_{i-\frac{1}{2}} + 6\left(\mathbf{F}_i - \mathbf{F}_{i+1}\right)\left(J\xi_x\right)_{i+\frac{1}{2}} \\ &- 4\left(\mathbf{F}_{i+1} - \mathbf{F}_{i+2}\right)\left(J\xi_x\right)_{i+\frac{3}{2}} + \left(\mathbf{F}_{i+2} - \mathbf{F}_{i+3}\right)\left(J\xi_x\right)_{i+\frac{5}{2}}\Big] \\ + \frac{1}{2}\mathbf{L}_{i+\frac{1}{2}} \cdot &\Big[\left(\mathbf{G}_{i-2} - \mathbf{G}_{i-1}\right)\left(J\xi_y\right)_{i-\frac{3}{2}} - 4\left(\mathbf{G}_{i-1} - \mathbf{G}_i\right)\left(J\xi_y\right)_{i-\frac{1}{2}} + 6\left(\mathbf{G}_i - \mathbf{G}_{i+1}\right)\left(J\xi_y\right)_{i+\frac{1}{2}} \\ &- 4\left(\mathbf{G}_{i+1} - \mathbf{G}_{i+2}\right)\left(J\xi_y\right)_{i+\frac{3}{2}} + \left(\mathbf{G}_{i+2} - \mathbf{G}_{i+3}\right)\left(J\xi_y\right)_{i+\frac{5}{2}}\Big] \\ + \frac{1}{2}\lambda\mathbf{L}_{i+\frac{1}{2}} \cdot &\Big[\left(\mathbf{U}_{i-2} - \mathbf{U}_{i-1}\right)\left(J\right)_{i-\frac{3}{2}} - 4\left(\mathbf{U}_{i-1} - \mathbf{U}_i\right)\left(J\right)_{i-\frac{1}{2}} + 6\left(\mathbf{U}_i - \mathbf{U}_{i+1}\right)\left(J\right)_{i+\frac{1}{2}} \\ &- 4\left(\mathbf{U}_{i+1} - \mathbf{U}_{i+2}\right)\left(J\right)_{i+\frac{3}{2}} + \left(\mathbf{U}_{i+2} - \mathbf{U}_{i+3}\right)\left(J\right)_{i+\frac{5}{2}}\Big],\end{aligned} \tag{16}$$

where Jacobians and metrics are defined at half-point, and $\left(J\right)_{i+\frac{1}{2}+k}$, $\left(J\xi_x\right)_{i+\frac{1}{2}+k}$ and $\left(J\xi_y\right)_{i+\frac{1}{2}+k}$, $k = -2, -1, 0, 1, 2$ are evaluated by the same sixth-order central scheme as Eq. (14).

When freestream is imposed, the primitive variables density ρ, velocity components u, v and pressure p are all constants. In Eq. (16), the local differences between adjoining cells are all zero, such as $\mathbf{F}_{i+1} - \mathbf{F}_i = 0$ and $\mathbf{U}_{i+1} - \mathbf{U}_i = 0$. Thus, the first term $\hat{f}_1^+$ in Eq. (13) vanishes.

Other terms in Eq. (13) can also be rewritten into local difference forms, which are

$$\begin{aligned}\hat{f}_2^+ &= (\mathbf{f}_{i-2}^+ - \mathbf{f}_{i-1}^+) - 7(\mathbf{f}_{i-1}^+ - \mathbf{f}_i^+) + 30(\mathbf{f}_i^+ - \mathbf{f}_{i+1}^+) - 7(\mathbf{f}_{i+1}^+ - \mathbf{f}_{i+2}^+) + (\mathbf{f}_{i+2}^+ - \mathbf{f}_{i+3}^+), \\ \hat{f}_3^+ &= (\mathbf{f}_{i+1}^+ - \mathbf{f}_i^+) - (\mathbf{f}_i^+ - \mathbf{f}_{i-1}^+), \\ \hat{f}_4^+ &= 16(\mathbf{f}_i^+ - \mathbf{f}_{i-1}^+) + 2(\mathbf{f}_{i-1}^+ - \mathbf{f}_{i-2}^+).\end{aligned}$$

These equations can be modified into GCLs-preserving forms as Eq. (16), similarly. Flux terms $\hat{f}_i^-, i = 1, 2, 3, 4$ can also be modified in the same way. Therefore, when freestream is imposed, the dissipation term in WENO-ZQ fluxes Eq. (12) vanishes.

In addition, to eliminate the error caused by metrics in non-linear weights, the smoothness indicators $\beta_1, \beta_2, \beta_3$ should also be rewritten into local difference forms for GCLs preservation. Here, we take β_1^+ as an illustration,

$$\begin{aligned}\beta_1^+ &= \frac{1}{144}\left(\left(f_{i-2}^+ - f_{i-1}^+\right) - 7\left(f_{i-1}^+ - f_i^+\right) - 7\left(f_i^+ - f_{i+1}^+\right) + \left(f_{i+1}^+ - f_{i+2}^+\right)\right)^2 \\ &+ \frac{1}{15600}\left(-11\left(f_{i-2}^+ - f_{i-2}^+\right) + 163\left(f_{i-1}^+ - f_i^+\right) - 163\left(f_i^+ - f_{i+1}^+\right) + 11\left(f_{i+1}^+ - f_{i+2}^+\right)\right)^2 \\ &+ \frac{781}{2880}\left(-\left(f_{i-2}^+ - f_{i-1}^+\right) + \left(f_{i-1}^+ - f_i^+\right) + \left(f_i^+ - f_{i+1}^+\right) - \left(f_{i+1}^+ - f_{i+2}^+\right)\right)^2 \\ &+ \frac{1421461}{1310400}\left(\left(f_{i-2}^+ - f_{i-1}^+\right) - 3\left(f_{i-1}^+ - f_i^+\right) + 3\left(f_i^+ - f_{i+1}^+\right) - \left(f_{i+1}^+ - f_{i+2}^+\right)\right)^2,\end{aligned} \tag{17}$$

where $f_k^+, k = i-2, ..., i+2$ are the components in the positive characteristic fluxes $\mathbf{f}_k^+$. These local difference forms of $\beta_1, \beta_2, \beta_3$ can be rewritten into the GCLs-preserving form as Eq. (16), similarly. Thus, the smoothness indicators are equal to zero for a uniform flow.

Proposition 2.1. *The sufficient conditions for the high-order WENO-ZQ scheme satisfying the GCLs property on curvilinear grids are that the error in the WENO-ZQ flux caused by the metric vanishes when freestream is imposed.*

Proof. The WENO-ZQ flux is split into a central component and a dissipation component as Eq. (12).

For the central component, the symmetrical conservative metric method (SCMM) [13] is applied to cancel out the error caused by the spatial metric.

The dissipation component is a combination of characteristic fluxes $\hat{f}_i^{\pm}$, and non-linear weights $\hat{\omega}_i^{\pm}, i = 1, ..., 4$. When freestream is imposed, the primitive variables density ρ, velocity components u, v and pressure p are all constants. On one hand, in Eq. (16), numerical fluxes on entire stencil $\mathbf{F}_k$ $\mathbf{G}_k$ and conservative variables $\mathbf{U}_k$ are constants, thus the difference between adjoining pair of fluxes equal to zeros, $\mathbf{F}_{k+1} - \mathbf{F}_k = 0$, $\mathbf{G}_{k+1} - \mathbf{G}_k = 0$, $\mathbf{U}_{k+1} - \mathbf{U}_k = 0, k = i-2, ..., i+3$, leading to $\hat{f}_1^{+} = 0$. Therefore, $\hat{f}_i^{\pm} = 0, i = 1, ..., 4$ is satisfied. On the other hand, non-linear weights $\hat{\omega}_i^{\pm}$ are calculated by Eq. (10) based on the smoothness indicators $\beta_i^{\pm}, i = 1, ..., 3$. Taking β_1^{+} as an example, Eq. (17) can be modified into a GCLs-preserving form as Eq. (16). Similarly, $\beta_i^{\pm} = 0$ is satisfied in a uniform flow field, leading to non-linear weights $\omega_i^{\pm}$ vanishing. Thus, the dissipation component equals to zero. The error in WENO-ZQ flux caused by the metric vanishes when freestream is imposed. ☐

Remark 2.1. On curvilinear grids, the present modified WENO-ZQ scheme preserves the GCLs property. Additionally, this modified GCLs-preserving WENO-ZQ scheme is equivalent to the WENO-ZQ scheme on Cartesian grids.

2.4. Discretization for the spatial metrics and the Jacobian

To obtain the cell-centered fluxes in ξ and η-direction, the metrics $x_\xi, y_\xi, x_\eta, y_\eta$ are required. According to [12], all of the above-mentioned derivatives must be computed using the unique scheme with at least fifth-order accuracy, which is the so-called symmetrical conservative metric method. As an example, we describe the calculation of x_ξ at the cell center (ξ_i, η_j). First, we compute the value at the cell face $\hat{x}_{i+1/2}$. Considering the stencil $\left(x_{i-2}, x_{i-1}, x_i, x_{i+1}, x_{i+2}, x_{i+3}\right)$, the same central scheme as the central part Eq. (12) is applied to generate the cell face value $\hat{x}_{i+1/2}$. We denote the reconstruction as

$$\hat{x}_{i+\frac{1}{2}} = \frac{1}{60}\left(x_{i-2} - 8x_{i-1} + 37x_i + 37x_{i+1} - 8x_{i+2} + x_{i+3}\right). \tag{18}$$

Similarly, the cell face value $\hat{x}_{i-1/2}$ can be also obtained with the stencil $\left(x_{i-3}, x_{i-2}, x_{i-1}, x_i, x_{i+1}, x_{i+2}\right)$ using the same reconstruction method,

$$\hat{x}_{i-\frac{1}{2}} = \frac{1}{60}\left(x_{i-3} - 8x_{i-2} + 37x_{i-1} + 37x_i - 8x_{i+1} + x_{i+2}\right). \tag{19}$$

Then the numerical derivation x_ξ at cell center (ξ_i, η_j) is obtained by

$$\left(x_\xi\right)_{i,j} = \frac{\hat{x}_{i+\frac{1}{2}} - \hat{x}_{i-\frac{1}{2}}}{\Delta\xi}, \tag{20}$$

where $\Delta\xi$ is the mesh spacing in ξ-direction.

As in [32], the symmetric conservation form of metrics is used to obtain Jacobian which is as

$$J = \frac{1}{2}\left[\left(J\xi_x x + J\xi_y y\right)_\xi + \left(J\eta_x x + J\eta_y y\right)_\eta\right]. \tag{21}$$

3. An adaptive multi-resolution method on curvilinear grids

The solution of the Euler equations exhibits a wide range of spatial and temporal scales, such as contact discontinuities and shock waves. For speedup, the adaptive multi-resolution method is invented in Cartesian coordinate systems, which increases the simulation resolution adaptively and reduces the computational time and memory cost. In this section, the adaptive multi-resolution method is extended to curvilinear coordinate systems. The high-order scheme is implemented on adaptive curvilinear grids.

3.1. Overview of the adaptive multi-resolution algorithms

The main principle of the adaptive multi-resolution representation is that the data given on a fine grid is represented as values on a coarser grid plus a series of differences at different levels of nested dyadic grids. On overlapping nested dyadic grids, the wavelet-based cell-averaged multi-resolution representation of a function $u(x,t)$ is written as

$$u(x,t) = \sum_k c_k \varphi_k(x,t) + \sum_k \sum_l d_{k,l} \psi_{k,l}(x,t), \tag{22}$$

where subscript k indicates all the grid points, l indicates the level of the nested dyadic grids which satisfies $l \to \infty$. In the first term, c_k are the scaling coefficients and $\varphi_k(x,t)$ are the scaling functions. In the second term, $d_{k,l}$ and $\psi_{k,l}(x,t)$ are the details and the wavelet functions, respectively.

In order to maintain conservation, two operators, namely the projection operator and the prediction operator, are utilized to transfer data between grids of different levels. These operators were originally designed by Bihari and Harten [5]. In one dimension, a projection operator $\mathbf{P}_{l+1\to l}$ is introduced to calculate the cell-averaged data of level l from level $l+1$, which is as

$$\mathbf{P}_{l+1\to l} : \bar{u}_j^l = \frac{1}{2}\left(\bar{u}_{2j}^{l+1} + \bar{u}_{2j+1}^{l+1}\right).$$

Here, the superscript l denotes the level and subscript j is the index of grid. The projection operator is unique and exact.

Besides, the prediction operator $\mathbf{P}_{l\to l+1}$ is used to estimate the cell-averaged data of level $l+1$ from level l, which is as

$$\mathbf{P}_{l\to l+1}: \quad \hat{u}^{l+1}_{2j} = \bar{u}^{l}_{j} + \sum_{i=1}^{2} \alpha_i \left(\bar{u}^{l}_{j+i} - \bar{u}^{l}_{j-i}\right),$$

$$\hat{u}^{l+1}_{2j+1} = \bar{u}^{l}_{j} - \sum_{i=1}^{2} \alpha_i \left(\bar{u}^{l}_{j+i} - \bar{u}^{l}_{j-i}\right),$$

where α_i is the interpolation coefficients that control the accuracy. To achieve fifth-order spatial accuracy, the coefficients are defined as $\alpha_1 = -\frac{22}{128}$, $\alpha_2 = \frac{3}{128}$. The prediction operator is non-unique and $\hat{u}$ is an approximation value.

The detail for a given grid point is defined as the difference between its projection value and prediction value, $d^l_j = \bar{u}^l_j - \hat{u}^l_j$. Adaptive mesh refinement or coarsening is achieved through comparison of this detail with a level-dependent threshold.

The multi-resolution algorithm consists of three parts, refinement, evolution and coarsening.

In the refinement step, the multi-resolution analysis is implemented on all leaf nodes in order to compute the details using the projection operator and the prediction operator. When a block's details are more than the refinement threshold, it is refined.

In the evolution step, a two-step TVD Runge-Kutta method with a local time-stepping algorithm is applied to increase efficiency and accuracy. Assuming that the time step in the block at the finest level is Δt, the time step in the coarsest block is $dt = 2^{L_{\text{finest}}}\Delta t$. Each block is integrated with its own level-dependent time step, i.e. the coarser blocks are integrated with larger time steps while finer blocks are integrated with small time step. With the help of the parallel technique, the blocks on different levels may be simultaneously updated.

And in the coarsening step, the coarsening operator is executed to remove the leaf block when its detail is sufficient less than the coarsening threshold, as determined by the multi-resolution analysis.

The multi-resolution algorithm comprises three primary components: refinement, evolution, and coarsening. First, in the refinement stage, multi-resolution analysis is performed on all leaf nodes to compute details using both projection and prediction operators. Blocks exceeding the refinement threshold undergo further refinement. Second, in the evolution stage, a two-step total variation diminishing (TVD) Runge-Kutta method is employed with local time-stepping to boost efficiency and accuracy. Given a time step Δt at the finest level block, the time step in the coarsest block is set to $dt = 2^{L_{\text{finest}}}\Delta t$. Integration for each block occurs independently with its own level-dependent time step. Coarser blocks are integrated using larger time steps while finer blocks are integrated using smaller time steps. With the help of parallel processing, blocks at different levels can be updated simultaneously. Finally, in the coarsening stage, the coarsening operator is utilized to remove leaf blocks whose details fall below the coarsening threshold determined by the multi-resolution analysis. This process improves computational efficiency without sacrificing accuracy.

3.2. The multi-resolution analysis on curvilinear grids

The multi-resolution analysis is utilized to estimate errors between distinct level grids using both projection and prediction operators. We extend these operators to work with curvilinear meshes. The conservative variables $\mathbf{U}$ in the physical domain are transformed into conservative variables $\widetilde{\mathbf{U}} = \boldsymbol{J}\mathbf{U}$ which contain Jacobian and spatial metrics in the computational domain.

Once the data at the $l+1$ level is computed in the computational domain, the projection operator $\mathbf{P}_{l+1\to l}$ is used to update the data at the l level, which is as follows:

$$\mathbf{P}_{l+1\to l} : (\overline{\boldsymbol{J}\mathbf{U}})^{l}_{j} = \frac{1}{2}\left((\overline{\boldsymbol{J}\mathbf{U}})^{l+1}_{2j} + (\overline{\boldsymbol{J}\mathbf{U}})^{l+1}_{2j+1}\right).$$

As the Jacobian is continuous and differentiable, the projection operator is unique and exact. The prediction operator, on the other hand, transfers the data from l level to $l+1$ level through a central interpolation of cell averages, defined as follows.

$$\mathbf{P}_{l\to l+1}: \quad (\widehat{\boldsymbol{J}\mathbf{U}})^{l+1}_{2j} = (\overline{\boldsymbol{J}\mathbf{U}})^{l}_{j} + \sum_{i=1}^{2} \alpha_i \left((\overline{\boldsymbol{J}\mathbf{U}})^{l}_{j+i} - (\overline{\boldsymbol{J}\mathbf{U}})^{l}_{j-i}\right),$$

$$(\widehat{\boldsymbol{J}\mathbf{U}})^{l+1}_{2j+1} = (\overline{\boldsymbol{J}\mathbf{U}})^{l}_{j} - \sum_{i=1}^{2} \alpha_i \left((\overline{\boldsymbol{J}\mathbf{U}})^{l}_{j+i} - (\overline{\boldsymbol{J}\mathbf{U}})^{l}_{j-i}\right),$$

where the interpolation coefficients α_i are as $\alpha_1 = -\frac{22}{128}$, $\alpha_2 = \frac{3}{128}$. The prediction operator is an approximation.

In two dimensions, the projection operator $\mathbf{P}_{l+1\to l}$ is as follows.

$$\mathbf{P}_{l+1\to l} : (\overline{\boldsymbol{J}\mathbf{U}})^{l}_{j,k} = \frac{1}{4}\left((\overline{\boldsymbol{J}\mathbf{U}})^{l+1}_{2j,2k} + (\overline{\boldsymbol{J}\mathbf{U}})^{l+1}_{2j+1,2k} + (\overline{\boldsymbol{J}\mathbf{U}})^{l+1}_{2j,2k+1} + (\overline{\boldsymbol{J}\mathbf{U}})^{l+1}_{2j+1,2k+1}\right).$$

The prediction operator $\mathbf{P}_{l\to l+1}$ in two dimensions is a locally central interpolation, defined as follows.

$$\mathbf{P}_{l\to l+1} : (\overline{\boldsymbol{J}\mathbf{U}})^{l+1}_{j+p,k+q} = (\overline{\boldsymbol{J}\mathbf{U}})^{l}_{j,k} - s_p\mathbf{T}_x - s_q\mathbf{T}_y + s_p s_q\mathbf{T}_{xy}. \tag{23}$$

Here, $\mathbf{T}_x, \mathbf{T}_y$ and $\mathbf{T}_{xy}$ represent temporary differences that are

$$\mathbf{T}_x = \sum_{p=1}^{2} \alpha_p \left((\overline{J\mathbf{U}})^l_{j+p,k} - (\overline{J\mathbf{U}})^l_{j-p,k} \right), \tag{24}$$

$$\mathbf{T}_y = \sum_{p=1}^{2} \alpha_p \left((\overline{J\mathbf{U}})^l_{j,k+p} - (\overline{J\mathbf{U}})^l_{j,k-p} \right), \tag{25}$$

$$\mathbf{T}_{xy} = \sum_{p=1}^{2} \sum_{q=1}^{2} \alpha_p \alpha_q \left((\overline{J\mathbf{U}})^l_{j+p,k+q} - (\overline{J\mathbf{U}})^l_{j+p,k-q} - (\overline{J\mathbf{U}})^l_{j-p,k+q} + (\overline{J\mathbf{U}})^l_{j-p,k-q} \right). \tag{26}$$

To minimize errors resulting from metrics and Jacobian and maintain the GCLs property, we take $\mathbf{T}_x$ as an example. Firstly, we reformulated Eq. (24) using a local difference form as Eq. (13),

$$\begin{aligned}
\mathbf{T}_x = \alpha_1 \Big[& \left((\overline{J\mathbf{U}})^l_{j+1,k} - (\overline{J\mathbf{U}})^l_{j,k} \right) + \left((\overline{J\mathbf{U}})^l_{j,k} - (\overline{J\mathbf{U}})^l_{j-1,k} \right) \Big] \\
+ \alpha_2 \Big[& \left((\overline{J\mathbf{U}})^l_{j+2,k} - (\overline{J\mathbf{U}})^l_{j+1,k} \right) + \left((\overline{J\mathbf{U}})^l_{j+1,k} - (\overline{J\mathbf{U}})^l_{j,k} \right) \\
& + \left((\overline{J\mathbf{U}})^l_{j,k} - (\overline{J\mathbf{U}})^l_{j-1,k} \right) + \left((\overline{J\mathbf{U}})^l_{j-1,k} - (\overline{J\mathbf{U}})^l_{j-2,k} \right) \Big].
\end{aligned} \tag{27}$$

By using the metrics and Jacobian defined at half-point, we modify Eq. (27) into a GCLs-preserving form as Eq. (16),

$$\begin{aligned}
\mathbf{T}_x = \alpha_1 \Big[& \left((\overline{\mathbf{U}})^l_{j+1,k} - (\overline{\mathbf{U}})^l_{j,k} \right) J_{j+\frac{1}{2},k} + \left((\overline{\mathbf{U}})^l_{j,k} - (\overline{\mathbf{U}})^l_{j-1,k} \right) J_{j-\frac{1}{2},k} \Big] \\
+ \alpha_2 \Big[& \left((\overline{\mathbf{U}})^l_{j+2,k} - (\overline{\mathbf{U}})^l_{j+1,k} \right) J_{j+\frac{3}{2},k} + \left((\overline{\mathbf{U}})^l_{j+1,k} - (\overline{\mathbf{U}})^l_{j,k} \right) J_{j+\frac{1}{2},k} \\
& + \left((\overline{\mathbf{U}})^l_{j,k} - (\overline{\mathbf{U}})^l_{j-1,k} \right) J_{j-\frac{1}{2},k} + \left((\overline{\mathbf{U}})^l_{j-1,k} - (\overline{\mathbf{U}})^l_{j-2,k} \right) J_{j-\frac{3}{2},k} \Big].
\end{aligned} \tag{28}$$

When the freestream is imposed, the conservative variables at all cell center are constants, $\overline{\mathbf{U}}^l_{i,j} = \text{constant}$, and Eq. (28) vanishes. The same approach used for T_x can be applied to T_y and T_{xy} in a similar manner. The Jacobian and metrics at the midpoints of T_x, T_y and T_{xy} are evaluated using the identical high-order central scheme as in Eq. (14). Therefore, the prediction operator preserves the GCLs property.

Proposition 3.1. *The sufficient conditions for the MR method achieving high-order spatial accuracy on multi-level curvilinear grids are that the error caused by the metric vanishes in the numerical algorithm on each finest grid and in the data transfer between different levels of grid when freestream is imposed.*

Proof. In the adaptive MR method, data is stored on multi-level curvilinear grids and the numerical algorithm is processed on each finest grid.

On one hand, on each finest grid, the proposed fifth-order GCLs-preserving WENO-ZQ scheme is applied to achieve high-order accuracy numerical solutions. According to the proof of the Proposition 2.1, the error caused by the metric is not longer generated when freestream is imposed.

On the other hand, with the fifth-order GCLs-preserving predictor operator mentioned above, the error due to the metric equals to zero when freestream is imposed. Hence, the data transfer from coarse grid to fine grid preserves high-order accuracy. Besides, the projection operator is unique and exact, leading to the error caused by the metric vanishing in the data transfer from fine grid to coarse grid.

Thus, the error from the metric is canceled in the data transfer between different levels of grid when in a uniform flow field. ☐

The prediction coefficients are as $\alpha_1 = \frac{-22}{128}, \alpha_2 = \frac{3}{128}$. And the coefficients $s_r = (-1)^{r+1},\ r = p, q$.

In the refinement step, the multi-resolution analysis is employed to evaluate the details on all leaf nodes. Assume that a block at level l contains $N \times N$ cells, its details are obtained by $d^l_{i,j} = \bar{u}^l_{i,j} - \hat{u}^l_{i,j}, i, j = 1, ..., N$. When the detail of any cell in the block exceeds a level-dependent refinement threshold $\forall d^l_{i,j} > \varepsilon^l$, that corresponding block should be refined. From error analysis [9,35], the refinement threshold at level l is chosen to be

$$\varepsilon^l = 2^{d_0(l-L_{\max})}\varepsilon, \tag{29}$$

where $L_{\max}$ is the maximum level of adaptive nested dyadic grids and d_0 is the space dimension. In our numerical tests, the prescribed threshold ε in Eq. (29) equals to 0.01.

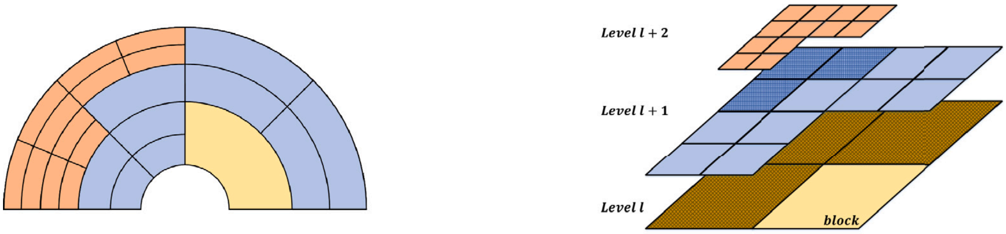

(a) Physical grids. (b) Data structure.

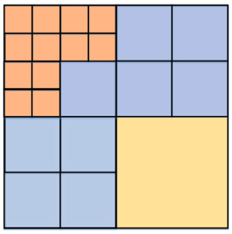

(c) Computational grids.

Fig. 1. Schematic for pyramid data structure. Fig. 1(a) is the mesh in the physical domain and Fig. 1(c) is the mesh in the computational domain. Fig. 1(b) is the schematic for pyramid data structure from level l to $l+2$. Each block contains predefined number of cells. The yellow, blue and red blocks represent the blocks at level l, $l+1$ and $l+2$, respectively. (For interpretation of the colors in the figure(s), the reader is referred to the web version of this article.)

3.3. Data structure

In the adaptive multi-resolution method, a pyramid data structure is utilized, as depicted in Fig. 1. Blocks, each containing a fixed number of cells, are defined within this structure; in our numerical examples, these blocks contain 16×16 cells in two dimensions. Compared to a tree data structure, the pyramid structure simplifies the process of identifying neighboring and parent blocks, thus facilitating efficient and convenient parallel algorithm execution. Physical variables and governing equations on curvilinear grids in the physical domain are transformed into Cartesian grids in the computational domain, with the pyramid data structure being constructed through the multi-resolution analysis method. To solve transformed governing equations in the leaf blocks of the computational domain, we apply the fifth-order GCLs-preserving WENO-ZQ scheme and the TVD Runge-Kutta local time stepping method. The GCLs-preserving projection and prediction operators are used to update data at different levels in the pyramid data structure.

4. Numerical results

In this section, the following numerical examples demonstrate the potential of the high-order adaptive multi-resolution method for compressible Euler equations on curvilinear grids. All the cases are performed with 28 Inter(R) Xeon(R) Gold 6132 CPU @ 2.60 GHz cores and 12*8 GB DDR4 2400 MHz ECC memory. The fifth-order GCLs-preserving WENO-ZQ scheme with a space-time adaptive multi-resolution algorithm and a TVD Runge-Kutta method are applied to all the examples.

A series of one and two-dimensional cases are tested:

Case 1. Accuracy and GCLs tests.

In this case, an accuracy test is presented to verify the order of the accuracy. Firstly, we begin with a one-dimensional accuracy test, where the physical domain is $[0,2]$ and the computational domain is $[0,2]$. Periodic boundary conditions are used at the left and right boundaries. The initial conditions are

$$(\rho, u, p) = (1 + 0.2\sin(\pi x), 1, 1).$$

The exact solutions are

$$\begin{cases} \rho(x,t) = 1 + 0.2\sin(\pi(x-t)), \\ u(x,t) = 1, \\ p(x,t) = 1. \end{cases}$$

The coordinate transformation between the physical domain and the computational domain is given as

$$x = \xi + 0.05\sin(\pi\xi),$$

where x is the spatial coordinate of the physical domain and ξ is the spatial coordinate of the computational domain. The L_1, L_2, L_∞ errors and corresponding orders of accuracy at $t = 2$ without and with adaptive multi-resolution method are presented in Table 1 and Table 2, respectively.

Table 1
Accuracy test: 1D advection of density perturbation with a nonuniform mesh at $t = 2$.

N	L_1 error	order	L_2 error	order	L_∞ error	order
50	2.6911E-07	-	2.9915E-07	-	4.2314E-07	-
100	8.3051E-09	5.0180	9.2256E-09	5.0191	1.3050E-08	5.0190
200	2.5868E-10	5.0047	2.8733E-10	5.0049	4.0636E-10	5.0052
400	8.0753E-12	5.0015	8.9695E-12	5.0015	1.2799E-11	4.9886
800	2.5192E-13	5.0025	2.7957E-13	5.0038	3.9985E-13	5.0004

Table 2
Accuracy test: 1D advection of density perturbation with a nonuniform mesh via adaptive multi-resolution method at $t = 2$. The block at coarsest level contains 50 cells.

L_{max}	L_1 error	order	L_2 error	order	L_∞ error	order
0	6.2816E-08	-	9.3518E-08	-	3.8314E-07	-
1	1.9615E-09	5.0011	2.9036E-09	5.0094	1.1963E-08	5.0013
2	6.1081E-11	5.0051	9.0222E-11	5.0081	3.7665E-10	4.9892
3	1.9195E-12	4.9920	2.7994E-12	5.0103	1.1775E-11	4.9994
4	5.8840E-14	5.0277	8.7343E-14	5.0023	3.6623E-13	5.0069

Table 3
Accuracy test: 2D advection of density perturbation with coordinate transformation (30) at $t = 2$.

N	L_1 error	order	L_2 error	order	L_∞ error	order
50	1.2337E-04	-	1.9591E-04	-	8.8265E-04	-
100	5.0719E-06	4.6043	8.3322E-06	4.5553	3.8824E-05	4.5068
200	1.9114E-07	4.7298	3.1909E-07	4.7067	1.5275E-06	4.6677
400	6.5942E-09	4.8573	1.1403E-08	4.8064	5.5772E-08	4.7755
800	2.0636E-10	4.9980	3.6676E-10	4.9585	1.8737E-09	4.8955

Table 4
Accuracy test: 2D advection of density perturbation with coordinate transformation (31) at $t = 2$.

N	L_1 error	order	L_2 error	order	L_∞ error	order
50	8.7797E-04	-	1.1203E-03	-	3.3856E-03	-
100	3.8189E-05	4.5229	4.9020E-05	4.5144	1.5341E-04	4.4640
200	1.5538E-06	4.6193	2.0786E-06	4.5597	6.5248E-06	4.5553
400	5.5472E-08	4.8079	7.9050E-08	4.7167	2.5858E-07	4.6572
800	1.8636E-09	4.8956	2.9068E-09	4.7653	9.5737E-09	4.7554

Secondly, a two-dimensional accuracy test is presented. Periodic boundary conditions are used at all boundaries. The initial conditions are

$$(\rho, u, v, p) = (1 + 0.2\sin(\pi(x+y)), 1, 1, 1).$$

The exact solutions are

$$\begin{cases} \rho(x,y,t) = 1 + 0.2\sin(\pi(x+y-t)), \\ u(x,y,t) = 1, \ v(x,y,t) = 1, \\ p(x,y,t) = 1. \end{cases}$$

Here, we consider two coordinate transformations between the physical domain and the computation domain and the computational domain is $[0,2] \times [0,2]$. The first one is as

$$\begin{cases} x = \xi + 0.05\sin(2\pi\eta), \\ y = \eta + 0.05\sin(2\pi\xi). \end{cases} \tag{30}$$

The second one is defined as

$$\begin{cases} x = \xi + 0.2\sin(\pi\xi)\sin(\pi\eta), \\ y = \eta + 0.2\sin(\pi\xi)\sin(\pi\eta). \end{cases} \tag{31}$$

The L_1, L_2, L_∞ errors and corresponding orders of accuracy at $t = 2$ of transformations (30) and (31) are presented in Table 3 and Table 4, respectively. See also Fig. 2.

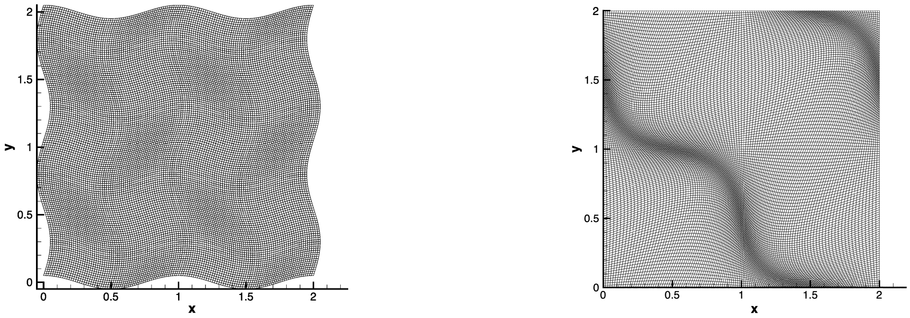

Fig. 2. 2D nonuniform mesh with coordinate transformation (30) and (31).

These accuracy tests have verified that our method can achieve fifth-order spatial accuracy.

Geometric conservation laws test.

In this test, the geometric conservation laws are tested on two-dimensional nonuniform grids which are obtained by the transformation (30). The initial condition is a free-stream condition, which is as,

$$(\rho, u, v, p) = (1, 1, 1, 1).$$

The L_1 errors of the velocities at $t = 0.5$ with 100 and 200 cells are 3.28×10^{-16} and 3.86×10^{-16}. These results indicate that our method preserves the geometric conservation laws, as the errors have vanished to machine zeros.

Case 2. One dimensional Riemann problem (Woodward-Colella Blast wave problem).

In this case, we consider the Woodward-Colella blast wave problem [41] on a nonuniform mesh. The physical domain is $[0, 1]$. And the computational domain is defined by the coordinate transformation as

$$x = \xi + 0.1 \sin(4\pi\xi), \quad \xi \in [0, 1]. \tag{32}$$

The initial states of the physical domain are as follows

$$\begin{cases} (\rho, u, p) = (1, 0, 1000), & x \in [0, 0.1), \\ (\rho, u, p) = (1, 0, 0.01), & x \in [0.1, 0.9), \\ (\rho, u, p) = (1, 0, 100), & x \in [0.9, 1]. \end{cases}$$

In this case, a reflective boundary condition is used at the left and right boundary. The numerical results with 416 cells at $t = 0.038$ are shown in Fig. 3.

The reference solution is computed by using 1600 cells on a uniform mesh. Initially, there are 16 cells. And with 6 times refinement, the finest resolution of the present method is $\Delta x = 1/1024$. At $t = 0.038$, the computation domain contains 416 cells by the present adaptive method. The results obtained by our adaptive method are in good agreement with the reference solutions. By utilizing the adaptive multi-resolution method, we can effectively identify and refine cells located at shock waves and contact discontinuities regions during the simulation.

Now, we consider the efficiency of the present method. From Fig. 4, we can see that as the resolution increase, the use of adaptive technique provides savings in cell count and computational time. At the same resolution, our method saves 90% of memory compared to the method without adaptive technique. This translates to a computational time savings of approximately 8 times than the non-adaptive method for one-dimensional problems. Furthermore, the growth ratio of our method is much less than the non-adaptive method.

Case 3. One dimensional Riemann problem (Shu-Osher shock interaction problem).

In this case, we consider the Shu-Osher shock interaction problem [34] on a nonuniform mesh. The physical domain is $[0, 10]$. And the computational domain is set by the coordinate transformation as

$$x = \xi + 0.1 \sin(\pi\xi/5), \quad \xi \in [0, 10]. \tag{33}$$

The initial states of the test are as follows

$$\begin{cases} (\rho, u, p) = (3.857143, 2.629369, 10.333333), & x \in [0, 1), \\ (\rho, u, p) = (1 + 0.2\sin(5(x - 5)), 0, 1), & x \in [1, 10). \end{cases}$$

In this case, an inflow boundary condition is imposed at the left boundary and an outflow boundary condition is used at the right boundary. The numerical results with 592 cells at $t = 1.8$ are shown in Fig. 5.

The reference solution is computed by using 1600 cells on a uniform mesh. Initially, there are 16 cells. And with 6 times refinement, the finest resolution of the present method is $\Delta x = 1/1024$. At $t = 1.8$, the computation domain contains 596 cells by the present adaptive method. The results by the adaptive method are in good agreement with the reference solutions, especially in the

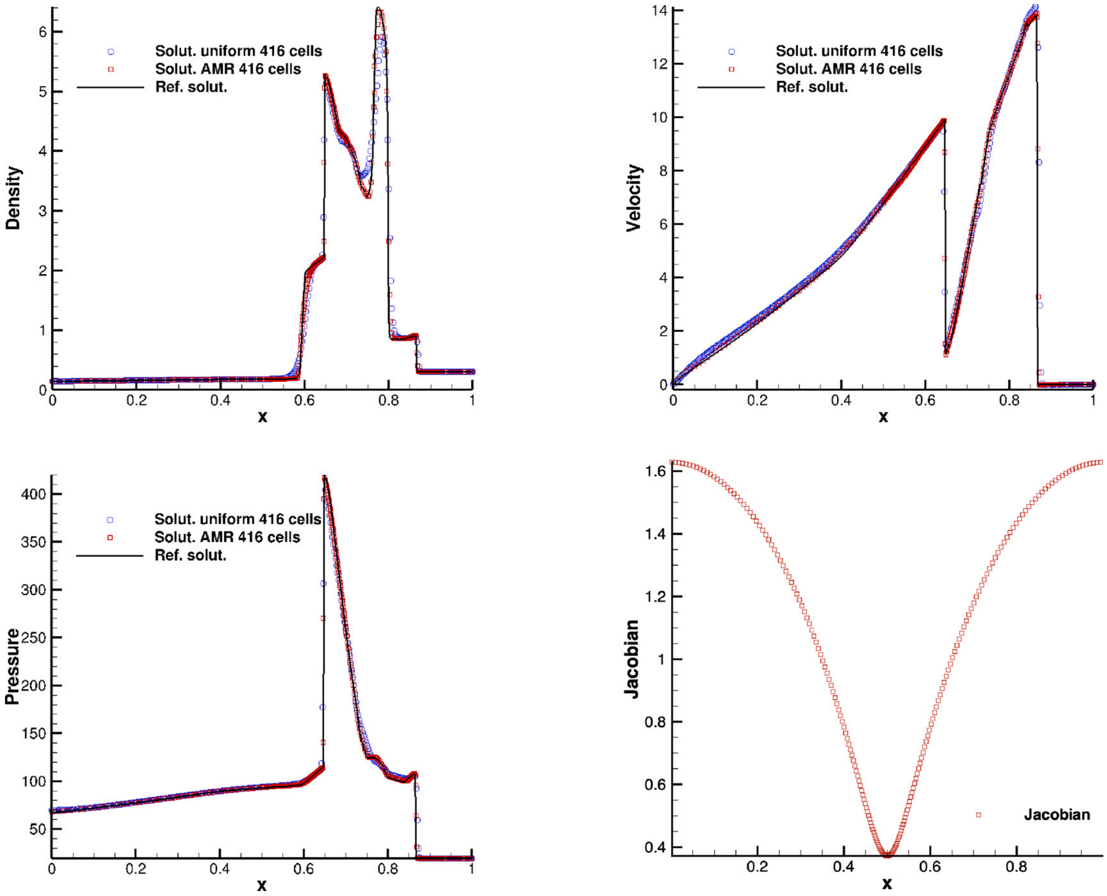

Fig. 3. Density, velocity, pressure and Jacobian distributions at $t = 0.038$, respectively. The red square markers represent the numerical results of our adaptive method. Initially, there are 16 cells. And with 6 times refinement, the finest resolution of the present method is $\Delta x = 1/1024$. At $t = 0.038$, the computation domain contains 416 cells by the present adaptive method. While the blue circle markers denote the results with 416 uniform cells. And the black lines are the reference solutions.

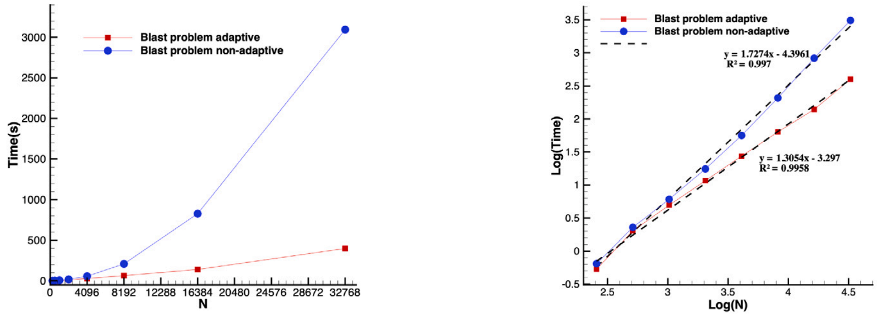

(a) Real time(s) vs Finest resolution.   (b) Log(time) vs Log(Finest resolution).

Fig. 4. The figures of the computation time of the blast problem. Fig. 4(a) shows the real computation time respect to the finest resolution from 256 to 32768 and Fig. 4(b) is the log(time) respect to the log(finest resolution). Within these two figures, the square symbol lines are the results with the adaptive MR method and the circle symbol lines are the results without the adaptive technique. The dash lines are the linear fitting lines.

high frequency area. With the help of the adaptive multi-resolution method, contact discontinuous and high frequency area detected and the cells nearby are refined to the finest resolution.

Case 4. Large density ratio problem.

In this case, we consider the large density ratio problem [38] on curvilinear grids. The physical domain is $[0, 100]$. And the computational domain is set by the coordinate transformation as

$$x = \xi + 0.1 \sin(\pi\xi/50). \quad \xi \in [0, 100]. \tag{34}$$

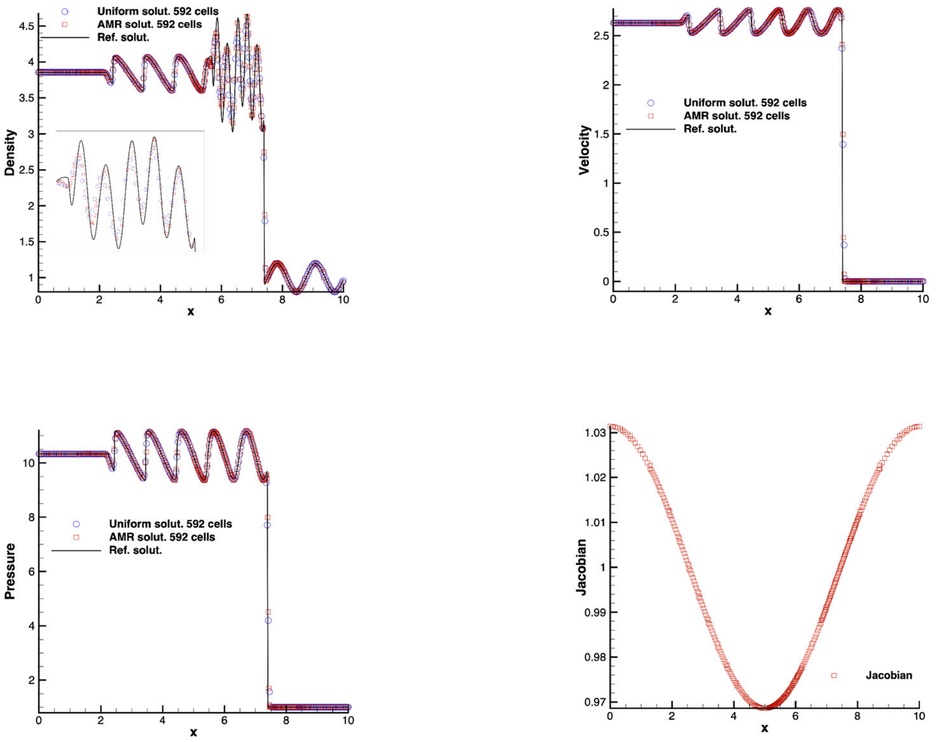

Fig. 5. Density, velocity, pressure and Jacobian distributions at $t = 1.8$, respectively. The red square markers are the numerical results of our adaptive method. Initially, there are 16 cells. And with 6 times refinement, the finest resolution of the present method is $\Delta x = 1/1024$. At $t = 1.8$, the computation domain contains 592 cells by the present adaptive method. While the blue circle markers denote the results with 592 uniform cells. And the black line is the reference solution.

The initial states of the test are as follows

$$\begin{cases} (\rho, u, p) = (10000, 0, 10000), & x \in [0, 30), \\ (\rho, u, p) = (1, 0, 1), & x \in [30, 100). \end{cases}$$

In this case, an inflow boundary condition is used at the left boundary and an outflow boundary condition is used at the right boundary. The numerical results with 1344 cells at $t = 0.15$ are shown in Fig. 6.

The reference solution is computed by using 20000 cells on a uniform mesh. Initially, there are 16 cells. And with 10 times refinement, the adaptive multi-resolution method captures the shock wave and the discontinuity with finest resolution $\Delta x = 1/16384$. At $t = 0.15$, the computation domain contains 1344 cells by the present adaptive method. From Fig. 6, for our adaptive method, with 1344 cells, the shock location converges to the correct position and the results are consistent well with the reference solution.

Case 5. Two-dimensional Riemann problem (four contact waves interaction).

In this instance, we consider a two-dimensional Riemann problem [25] on a nonuniform mesh. The physical domain is $[0, 2] \times [0, 2]$ and the computational domain is $[0, 2] \times [0, 2]$. The coordinate transformation between the physical domain and the computational domain is as

$$x = \xi + 0.05 \sin^2(2\pi\xi) \sin(\pi\eta),$$

$$y = \eta + 0.05 \sin(2\pi\xi) \sin^2(\pi\eta).$$

The initial states of the test are as follows

$$\begin{cases} (\rho, u, v, p) = (1, 0.75, -0.5, 0.5), & x > 0.5, y > 0.5, \\ (\rho, u, v, p) = (2, 0.75, 0.5, 0.5), & x < 0.5, y > 0.5, \\ (\rho, u, v, p) = (1, -0.75, 0.5, 0.5), & x < 0.5, y < 0.5, \\ (\rho, u, v, p) = (3, -0.75, -0.5, 0.5), & x > 0.5, y < 0.5. \end{cases}$$

In this case, all boundaries are reflective. The numerical results at the finest resolution 1024×1024 with 6 times adaptive refinement at $t = 0.5$ are shown in Fig. 7.

In this case, four contact discontinuities interact with each other and produce a vortex. Initially, there is only one block with 16×16 cells. Using the adaptive multi-resolution method, after 6 times refinement, the MR results use only 252160 cells with 985 blocks to achieve the finest resolution 1024×1024, which saves 76% computational cells. In this case, each block contains 16×16 cells. Comparing to the results in Fig. 7(b) of 252160 uniform cells, the numerical results of our method show more details around

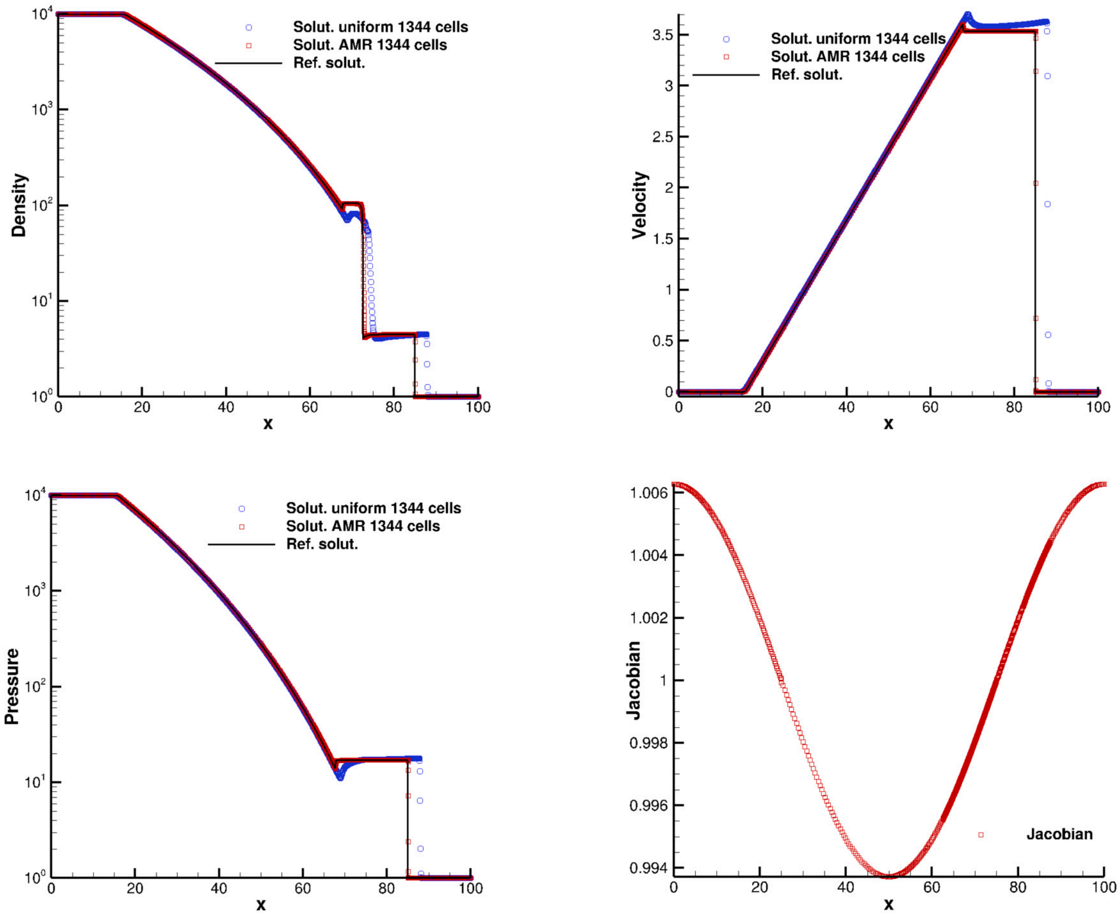

Fig. 6. Density, velocity, pressure and Jacobian distributions at $t = 12$, respectively. The red circle is the numerical results of our method with 1344 cells. The red square markers are the numerical results of our adaptive method. Initially, there are 16 cells. And with 10 times refinement, the finest resolution of the present method is $\Delta x = 1/16384$. At $t = 0.15$, the computation domain contains 1344 cells by the present adaptive method. While the blue circle markers denote the results with 1344 uniform cells. And the black line is the reference solution.

the vortex and the resolution of the contact discontinuity is higher. From Fig. 7(c) and Fig. 7(d), the blocks near the discontinuities are refined to the finest resolution.

Case 6. Two dimensional Riemann problem.

In this case, we consider a two-dimensional Riemann problem [36] on a nonuniform mesh. The physical domain is $[0,2] \times [0,2]$ and the computational domain is $[0,2] \times [0,2]$. The coordinate transformation between the physical domain and the computational domain is as

$$x = \xi + 0.05 \sin^2(\pi\xi) \sin(\pi\eta), \tag{35}$$

$$y = \eta + 0.05 \sin(\pi\xi) \sin^2(\pi\eta). \tag{36}$$

The initial states of the test are as follows

$$\begin{cases} (\rho,u,v,p) = (1.1, 0, 0, 1.1), & x > 0.5, y > 0.5, \\ (\rho,u,v,p) = (0.5065, 0.8939, 0, 0.35), & x < 0.5, y > 0.5, \\ (\rho,u,v,p) = (1.1, 0.8939, 0.8939, 1.1), & x < 0.5, y < 0.5, \\ (\rho,u,v,p) = (0.5065, 0, 0.8939, 0.35), & x > 0.5, y < 0.5. \end{cases}$$

In this case, all boundaries are reflective. The numerical results at the finest resolution 1024×1024 with 6 times refinement at $t = 0.5$ are shown in Fig. 8.

This case is the interaction between four shock waves. Initially, there is one block with 16×16 cells in the computational domain. With the help of the adaptive multi-resolution method, after 6 times refinement, the MR results use 295936 cells with 1156 blocks to achieve the finest resolution 1024×1024, which saves 71.8% computational cells. Each block contains predetermined 16×16 cells. Comparing to the results in Fig. 8(b) of 295936 uniform cells, the numerical results of our method show higher resolution near

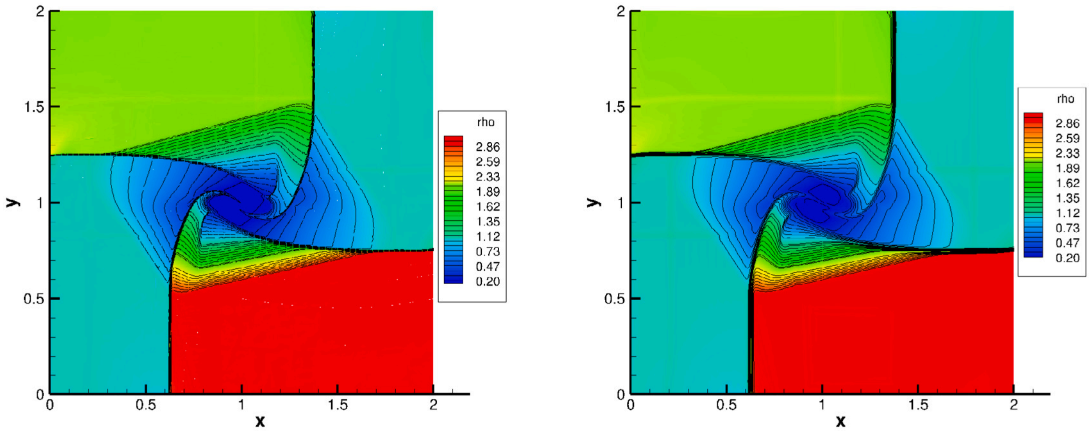

(a) AMR results (Density contour). (b) Uniform results (Density contour).

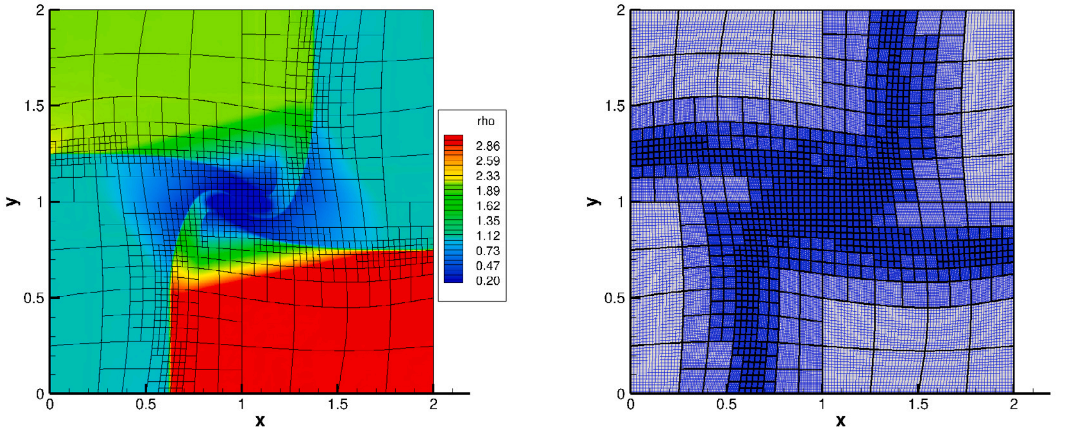

(c) Adaptive multi-resolution blocks. (d) Adaptive grids.

Fig. 7. Fig. 7(a) is the density distributions by our adaptive multi-resolution method with total 252160 cells and Fig. 7(b) is the density contour with the same amount uniform cells. Fig. 7(c) shows the adaptive blocks and each block contains 16×16 cells. Fig. 7(d) shows the adaptive curvilinear grids in the physical domain.

the shock waves. From Fig. 8(c) and Fig. 8(d), the blocks near the shock waves are identified and adaptively refined to the finest resolution.

Case 7. Two dimensional Riemann problem.

In this case, we consider a two-dimensional Riemann problem [36] on a nonuniform mesh. The physical domain is $[0,2] \times [0,2]$ and the computational domain is $[0,2] \times [0,2]$. The coordinate transformation between the physical domain and the computational domain is as

$$x = \xi + 0.05 \sin^2(\pi\xi) \sin(\pi\eta), \tag{37}$$

$$y = \eta + 0.05 \sin(\pi\xi) \sin^2(\pi\eta). \tag{38}$$

The initial states of the test are as follows

$$\begin{cases} (\rho, u, v, p) = (0.5313, 0, 0, 0.4), & x > 0.5, y > 0.5, \\ (\rho, u, v, p) = (1.0, 0.7276, 0, 1), & x < 0.5, y > 0.5, \\ (\rho, u, v, p) = (0.8, 0, 0, 1), & x < 0.5, y < 0.5, \\ (\rho, u, v, p) = (1, 0, 0.7276, 1), & x > 0.5, y < 0.5. \end{cases}$$

In this case, all boundaries are reflective. The numerical results at the finest resolution 512×512 with 5 times refinement at $t = 0.5$ are shown in Fig. 9. This case is the interaction between two shock waves and two contact discontinuities and a jet is formed. Initially, there is one block with 16×16 cells. With the help of the adaptive multi-resolution method, after 5 times refinement, the MR results use 118528 cells with 463 blocks to achieve the finest resolution 512×512, which saves 54.8% computational cells. Each block contains predetermined 16×16 cells. Comparing to the results in Fig. 9(b) of 118528 uniform cells, the numerical results of our method show higher resolution near the shock waves and the contact discontinuities and there are more detail of the jet. From

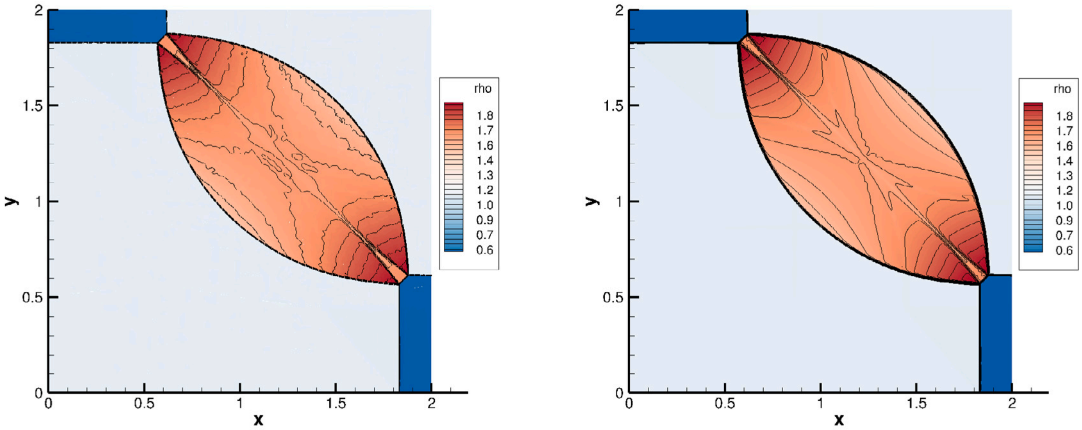

(a) AMR results (Density contour). (b) Uniform results (Density contour).

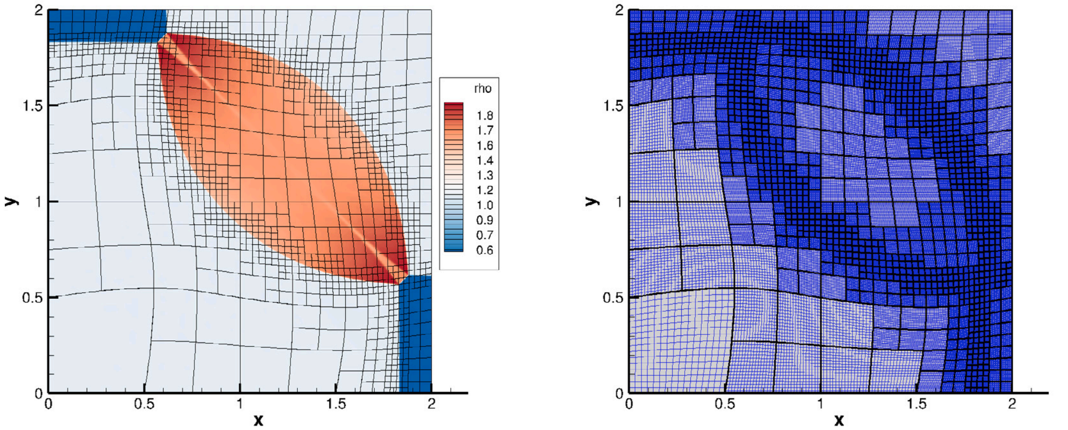

(c) Adaptive multi-resolution blocks. (d) Adaptive grids.

Fig. 8. Fig. 8(a) is the density distributions by our adaptive multi-resolution method with total 295936 cells and Fig. 8(b) is the density contour with the same amount uniform cells at a resolution 544 × 544. Fig. 8(c) shows the adaptive blocks and each block contains 16 × 16 cells. Fig. 8(d) shows the adaptive curvilinear grids in the physical domain.

Fig. 9(c) and Fig. 9(d), the blocks near the shock waves and the contact discontinuities are identified and adaptively refined to the finest resolution while the smooth area is represented by the coarsen blocks.

Case 8. Hypersonic flow past a cylinder.

In this case, we consider the hypersonic flow past a cylinder nonuniform mesh. The physical domain is a semicircle with radius $r = 1.5$ and the cylinder with radius $r = 0.5$ locates in the midpoint of the diameter. The computational domain is $[0.0, 1.0] \times [0.0, 1.0]$ and the coordinate transformation between the physical domain and the computational domain is as

$$x = (\xi + 0.5)\cos(\pi(\eta - 0.5)), \tag{39}$$

$$y = (\xi + 0.5)\sin(\pi(\eta - 0.5)). \tag{40}$$

In this case, a flow moving towards to a cylinder, initially. And the initial states are as follows

$$\begin{cases} (\rho, u, v, p) = (1, 0, 0, 1), & r < 1.48, \\ (\rho, u, v, p) = (1, u_{\text{Ma}}, 0, 1/1.4), & r \geq 1.48, \end{cases}$$

where $u_{\text{Ma}} = 5, 8, 10$ which denotes the Mach number of the flows with $\text{Ma} = 5, 8, 10$.

In this case, a reflective boundary condition is used at the surface of cylinder and an outflow boundary condition is used at the left boundary. The numerical results at the finest resolution 512×512 at the steady state with the Mach number $\text{Ma} = 5, 8, 10$ are shown in Fig. 10. In Fig. 10(a), the current MR method uses 106496 cells with 416 blocks to achieve 512×512 resolution, which saves 59.4% computational cells. Additionally, Fig. 10 shows that the current MR method has the ability to capture strong shock waves with high Mach number and also avoid the carbuncle phenomenon as in [33].

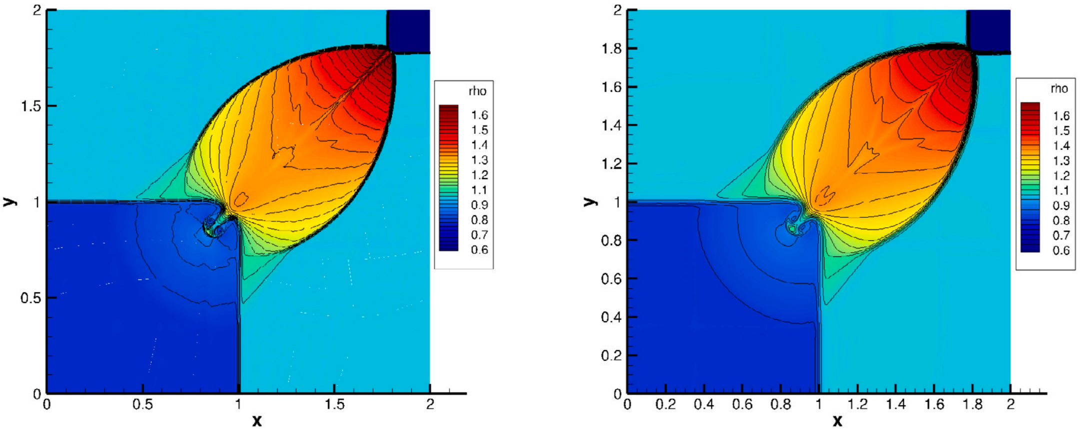

(a) AMR results (Density contour). (b) Uniform results (Density contour).

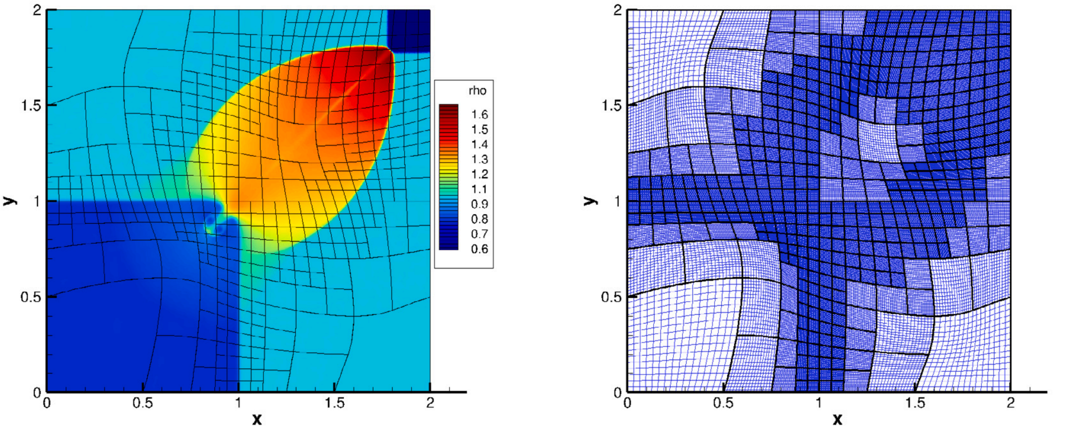

(c) Adaptive multi-resolution blocks. (d) Adaptive grids.

Fig. 9. Fig. 9(a) is the density distributions by our adaptive multi-resolution method with total 118528 cells and Fig. 9(b) is the density contour with the same amount uniform cells at a resolution 344×344. Fig. 9(c) shows the adaptive blocks and each block contains 16×16 cells. Fig. 9(d) shows the adaptive curvilinear grids in the physical domain.

Now, we consider the internal geometric configuration of the physical domain is elliptical with the long axis 0.5 and the short axis 0.3. The computation domain is $[0,1] \times [0,1]$. At the ellipse, the boundary condition is reflection condition and the right boundary condition is inflow condition. Outflow conditions are used for other boundaries. A free-stream of Mach 2.0 is imposed at time $t = 0$. Initially, the resolution is 16×16. After $L_{\max} = 5$ times refined, the numerical results at the finest 512×512 at the steady state are shown in Fig. 10.

At the steady state, there are 214 blocks which contains 54784 cells. The data compression ratio is 79.1%. As shown in Fig. 11, the shock waves are captured well. The robustness of the current MR method is validated on the anisotropy curvilinear grids.

Case 9. Double Mach reflection on a 30° wedge.

The double Mach reflection was studied by Woodward and Colella [41]. In this case, the double Mach reflection problem is solved on a 30° wedge. The physical domain is a 30° wedge with five vertexes $(0,0)$, $(\frac{\sqrt{3}}{12}+\frac{1}{2},0)$, $(0,\frac{\sqrt{3}}{3}(\frac{1}{4}-\frac{3}{12}))$, $(3,0)$, $(0,2)$. The grid points in the physical domain are smoothed. The computational domain is $[0,2] \times [0,1]$. Initially, the shock wave is at $x = x_0 = \sqrt{3}/12 + 0.25$ and the right-moving shock wave with Mach 10 impacts the wedge and leads to the double Mach reflection. The initial states are as follows

$$\begin{cases} (\rho,u,v,p) = (8.0, 8.25, 0, 116.5), & x < x_0, \\ (\rho,u,v,p) = (1.4, 0, 0, 1.0), & x \geq x_0. \end{cases}$$

In this case, an inflow boundary condition is used at the left boundary and an outflow boundary condition is used at the right boundary. And reflective boundary conditions are imposed at the bottom and the bevel boundary. If $x \leq s(t)$, states of the upper boundary are equal to initial post-shock states. If $x > s(t)$, states of the upper boundary are equal to initial pre-shock states. The numerical results at time $t = 0.2$ at the finest resolution 2048×1024 are shown in Fig. 12.

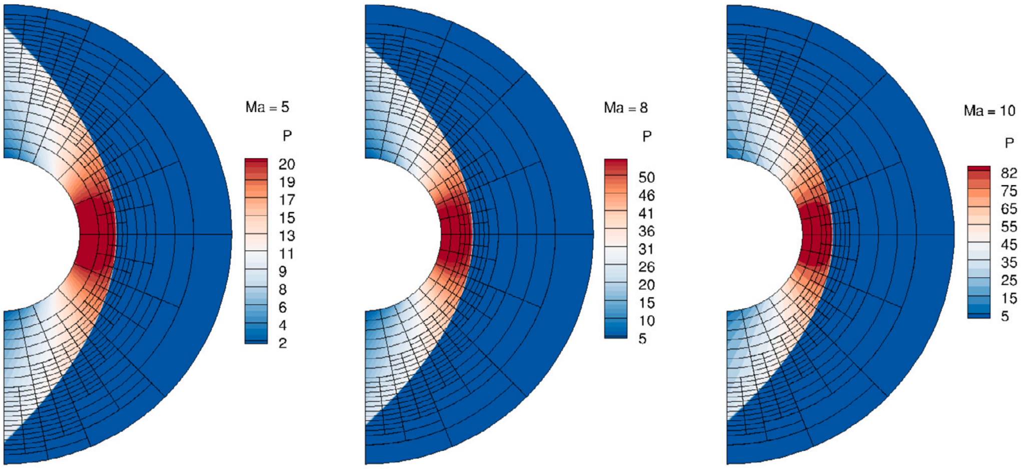

(a) Mach 5 flows. (b) Mach 8 flows. (c) Mach 10 flows.

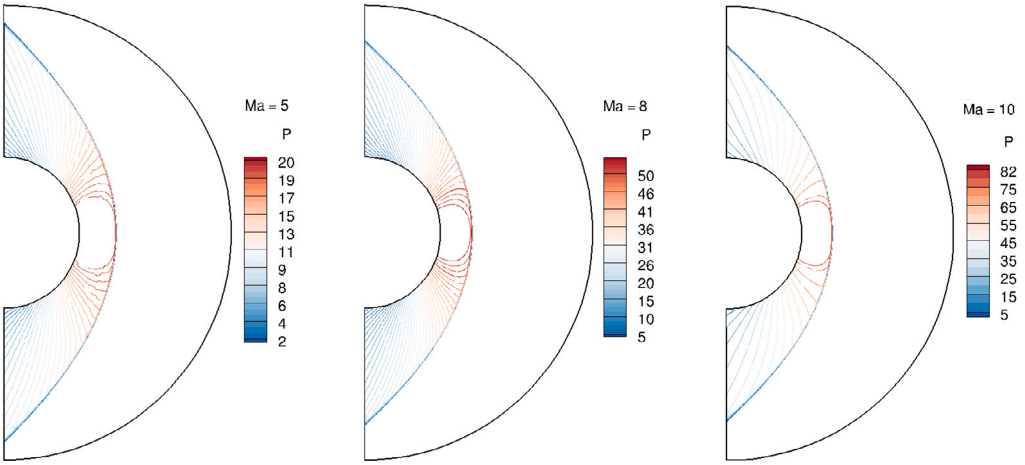

(d) Mach 5 flows. (e) Mach 8 flows. (f) Mach 10 flows.

Fig. 10. Pressure distributions with Mach 5, 8, 10 flows.

The CFL number is set to 0.4. Fig. 12(a) shows the density distributions with 40 contours from 1.88783 to 20.9144 and the Fig. 12(b) are the local enlargement of density contours. The adaptive physical grids are shown in Fig. 12(c) and the adaptive multi-resolution blocks are shown in Fig. 12(d). Initially, the resolution is 64×32. After adaptive refining $L_{\max} = 5$, at time $t = 0.2$, there are 458 blocks and 468992 cells in the domain. The data compression ratio is 79.2%. The adaptive multi-resolution method shows the shock-capturing ability on the curvilinear girds. Comparing to the results from Zhu and Qiu [44], the shock waves and discontinuities are captured well.

Case 10. The channel flow problem.

In this case, the two-dimensional channel flow problem is solved which was first studied by Casper et al. [6]. The physical domain is a channel and a C^3 geometry is considered, which means that the connections of the middle sections of the channel boundary to the other sections are continuous to third derivative in x. The middle sections of the channel boundary are determined by

$$\begin{cases} y_1(x) = -0.5 + 0.05\sin^4\left(\dfrac{10}{9}\pi x + \dfrac{\pi}{2}\right), y < 0, \\ y_2(x) = 0.5 - 0.05\sin^4\left(\dfrac{10}{9}\pi x + \dfrac{\pi}{2}\right), y > 0. \end{cases} \tag{41}$$

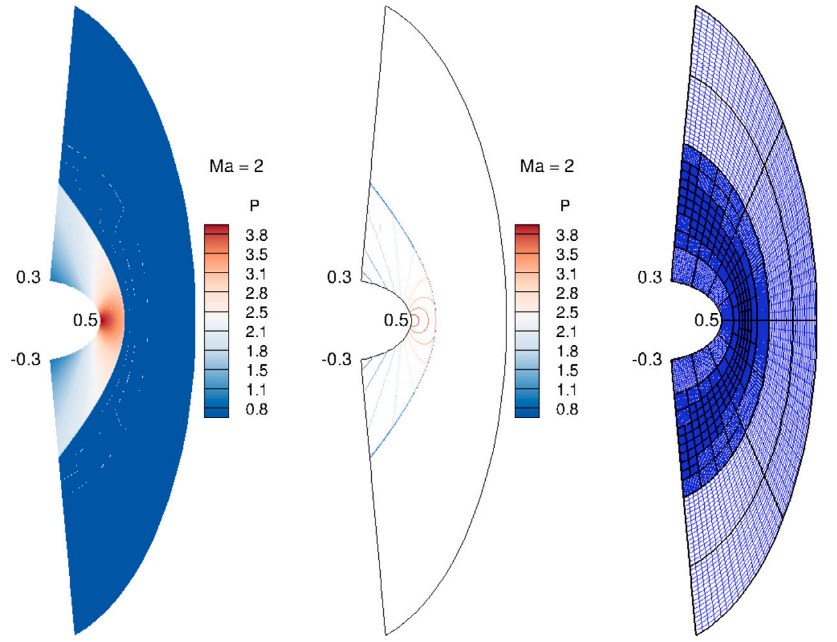

(a) Pressure distributions. (b) Pressure contours. (c) Adaptive grids.

Fig. 11. Pressure distributions. Here, 20 contours are drawn from 0.8 to 3.8.

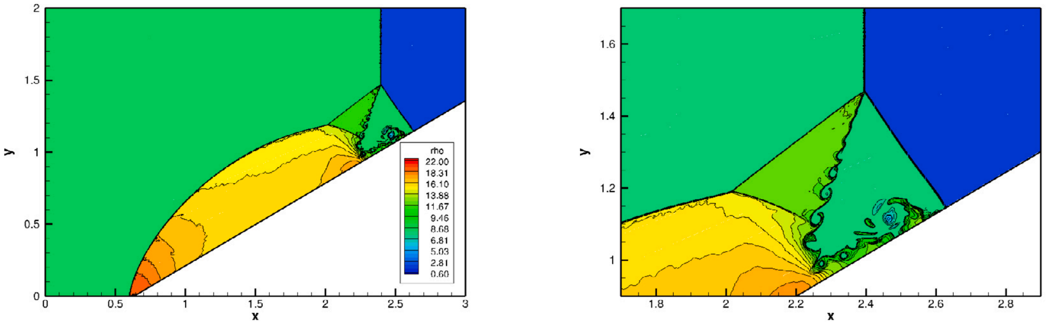

(a) Density contours. (b) Local enlargement of the density contours.

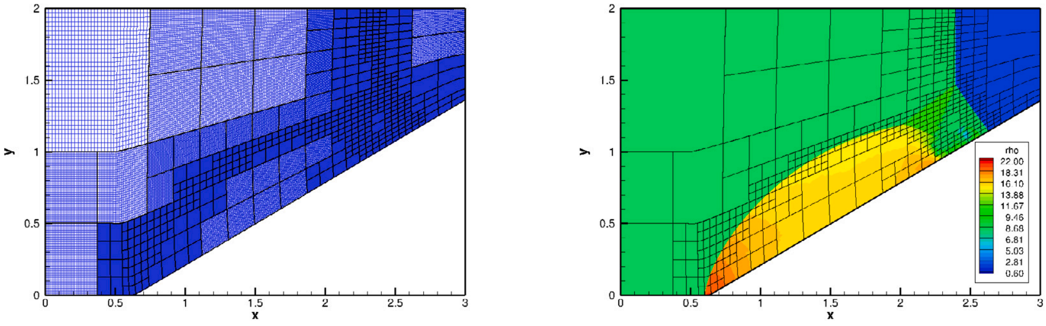

(c) Adaptive grids. (d) Adaptive multi-resolution blocks.

Fig. 12. Density distributions of the double Mach reflection on a 30° wedge. Here 30 contours are drawn from 0.6 to 22.0.

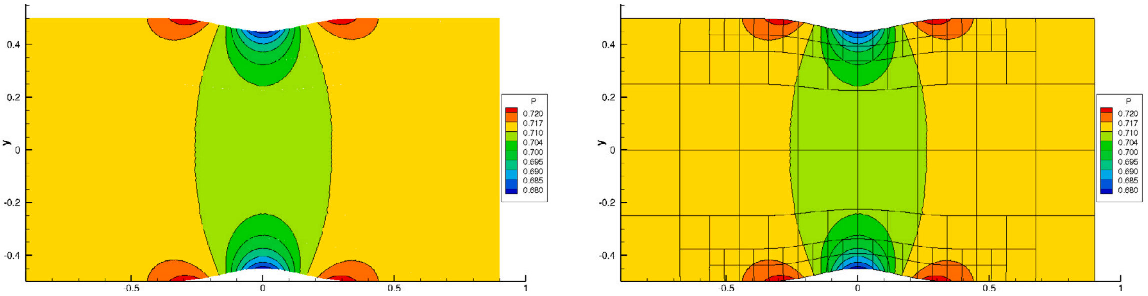

(a) Pressure contours. (b) Adaptive multi-resolution blocks.

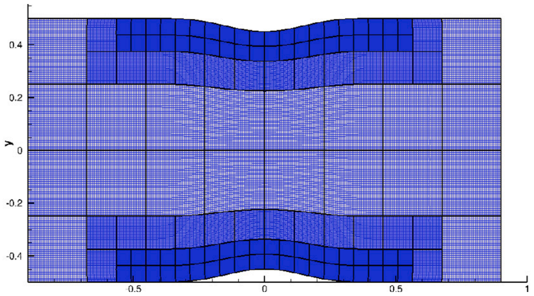

(c) Adaptive grids.

Fig. 13. The pressure distributions of the channel flow. The adaptive multi-resolution blocks and grids.

The computational domain is $[0,2] \times [0,1]$. Subsonic inflow boundary condition is used at the left boundary and subsonic outflow boundary is used at the right boundary. Reflective boundary conditions are used at the upper and lower boundaries. The initial conditions are

$$(\rho, u, v, p) = (1, 0.3, 0, 1/1.4).$$

The numerical results of Mach number 0.3 at the finest resolution 1024×512 are presented in Fig. 13.

In this case, the CFL number is set to 0.4. Fig. 13(a) displays the pressure distributions, while Fig. 13(b) and Fig. 13(c) show the adaptive multi-resolution blocks and adaptive physical grids. Initially, the resolution is 64×32, which means that there are 64 control points along the channel boundary. After being refined $L_{\max} = 4$ times, the present method achieves its finest resolution at 1024×512, containing a total of 128 blocks and 131072 cells within the domain. The data compression ratio is 75% which illustrates that the proposed adaptive method achieves high-resolution solution with a high data compression ratio. Compared to the results in [6,42], our adaptive method adaptively refines the grids near the channel boundary where entropy errors exceed the refinement threshold. Also, the results demonstrate that the freestream preservation of our method is achieved.

Case 11. The transonic flow over a NACA0012 airfoil.

In this case, the transonic flow over a NACA0012 airfoil problem is solved. The physical domain is a circle with radius $r = 0.25$ and the NACA0012 airfoil is set in the middle with zero angle of attack. The O-type mesh is considered as that in [24]. The computational domain is $[0,2] \times [0,1]$. The initial conditions are

$$(\rho, u, v, p) = (1, 0.8, 0, 1/1.4).$$

A reflective boundary condition is used at the NACA0012 airfoil. An inflow boundary condition is used at the circle with $x < 2.5$ and an outflow boundary condition is used at the circle with $x \geq 2.5$. The numerical results of Mach number 0.8 with zero angle of attack at the finest resolution 4096×2048 are presented in Fig. 14.

The CFL number is set to 0.4. Fig. 14(a) shows the Mach number distributions with 18 contours from 0.05 to 1.45. The adaptive multi-resolution blocks are shown in Fig. 14(b) and the adaptive physical grids are shown in Fig. 14(c). Initially, the resolution is 256×128, which means that there are 256 control points along the airfoil. After adaptive refining $L_{\max} = 5$ times, the finest resolution is 4096×2048, which contains 1564 blocks and 1601536 cells in the domain. The data compression ratio is 80.9% which indicates that the proposed adaptive method achieves high-resolution solutions with a high data compression ratio. Compared to the results in [2,7], the strong and weak shock waves are captured more clearly, which verifies the proposed adaptive method on general curvilinear grids with curved boundaries.

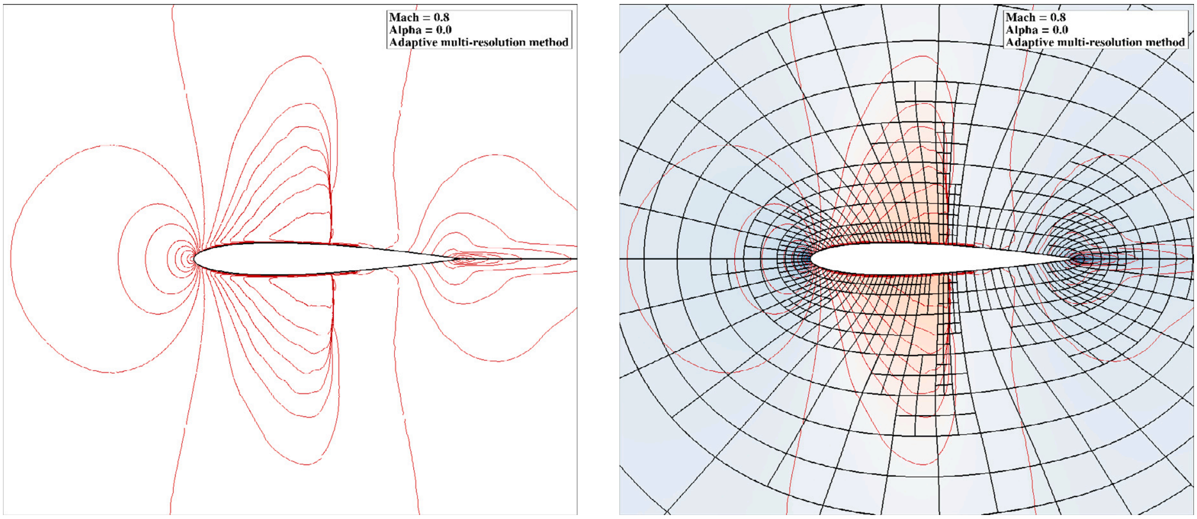

(a) The distributions of the Mach number.

(b) Adaptive multi-resolution blocks.

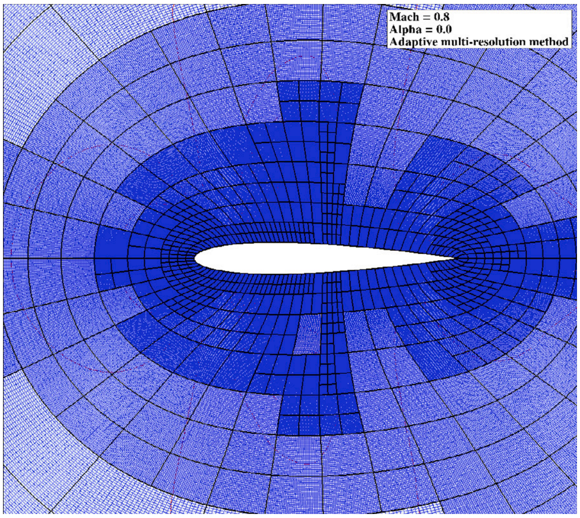

(c) Adaptive grids.

Fig. 14. Mach number distributions of the transonic flow over a NACA0012 airfoil. The adaptive multi-resolution blocks and grids.

5. Conclusion

In this work, a high-order adaptive multi-resolution method is developed on curvilinear grids to solve the hyperbolic conservation laws while preserving the geometric conservation laws (GCLs). First, the governing equations and the physical variables on curvilinear grids are transformed into Cartesian grids, containing geometric metrics. Then, a combination of the fifth-order GCLs-preserving finite difference WENO-ZQ scheme and adaptive multi-resolution method is proposed to solve the transformed governing equations. The proposed method deals with the metrics and Jacobians associated with the coordinate transformation meticulously while maintaining discrete GCLs to achieve designed high spatial accuracy and resolution. On the one hand, to achieve high-order spatial accuracy on curvilinear grids, a new fifth-order GCLs-preserving WENO-ZQ finite difference scheme is proposed for computing numerical fluxes. The numerical flux is split into a central component and a dissipation component, and reformulated into a modified local difference form to achieve GCLs preservation. On the other hand, the adaptive multi-resolution method (MR) is extended to curvilinear grids preserving GCLs. When constructing prediction and projection operators in the adaptive multi-resolution method, geometric metrics from the coordinate transformation are considered to reduce numerical errors. To accurately capture discontinuities and refine corresponding grids near them, metrics in the prediction operator are finely evaluated. One advantage of this method is the ability to avoid the complexity and difficulty of directly constructing high-order adaptive methods on curvilinear grids by carefully managing geometric metrics. The high-order accuracy, high resolution, and efficiency of the developed method are demonstrated with a broad set of benchmark tests in one and two space dimensions.

CRediT authorship contribution statement

Wenhua Ma: Conceptualization, Methodology, Software, Writing – original draft. **Dongmi Luo:** Methodology. **Shiyi Li:** Methodology. **Jianxian Qiu:** Methodology, Writing – review & editing. **Guoxi Ni:** Writing – review & editing. **Yibing Chen:** Conceptualization, Methodology, Supervision, Writing – review & editing.

Declaration of competing interest

The authors declare that they have no known competing financial interests or personal relationships that could have appeared to influence the work reported in this paper.

Data availability

Data will be made available on request.

Acknowledgements

This work is supported by National Key R&D Program of China (Grant Nos. 2022YFA1004500), NSFC (Grant Nos. 12271052, 11901044, 12101063, 12071392), National Key Project (Grant No. GJXM92579).

References

[1] Y. Abe, T. Nonomura, N. Iizuka, K. Fujii, Geometric interpretations and spatial symmetry property of metrics in the conservative form for high-order finite-difference schemes on moving and deforming grids, J. Comput. Phys. 260 (2014) 163–203.

[2] R. Abgrall, Essentially non-oscillatory residual distribution schemes for hyperbolic problems, J. Comput. Phys. 214 (2006) 773–808.

[3] A. Baeza, P. Mulet, Adaptive mesh refinement techniques for high-order shock capturing schemes for multi-dimensional hydrodynamic simulations, Int. J. Numer. Methods Fluids 52 (2006) 455–471.

[4] M.J. Berger, P. Colella, Local adaptive mesh refinement for shock hydrodynamics, J. Comput. Phys. 82 (1989) 64–84.

[5] B.L. Bihari, A. Harten, Multiresolution schemes for the numerical solution of 2-D conservation laws. I, SIAM J. Sci. Comput. 18 (1997) 315–354.

[6] J. Casper, C.-W. Shu, H. Atkins, Comparison of two formulations for high-order accurate essentially nonoscillatory schemes, AIAA J. 32 (1994) 1970–1977.

[7] H. Chen, C. Shu, An efficient implicit mesh-free method to solve two-dimensional compressible Euler equations, Int. J. Mod. Phys. C 16 (2005) 439–454.

[8] Y. Chen, G. Tóth, T.I. Gombosi, A fifth-order finite difference scheme for hyperbolic equations on block-adaptive curvilinear grids, J. Comput. Phys. 305 (2016) 604–621.

[9] A. Cohen, S. Kaber, S. Müller, M. Postel, Fully adaptive multiresolution finite volume schemes for conservation laws, Math. Comput. 72 (2003) 183–225.

[10] P. Colella, M.R. Dorr, J.A. Hittinger, D.F. Martin, High-order, finite-volume methods in mapped coordinates, J. Comput. Phys. 230 (2011) 2952–2976.

[11] R. Deiterding, M.O. Domingues, S.M. Gomes, K. Schneider, Comparison of adaptive multiresolution and adaptive mesh refinement applied to simulations of the compressible Euler equations, SIAM J. Sci. Comput. 38 (2016) S173–S193.

[12] X. Deng, M. Mao, G. Tu, H. Liu, H. Zhang, Geometric conservation law and applications to high-order finite difference schemes with stationary grids, J. Comput. Phys. 230 (2011) 1100–1115.

[13] X. Deng, Y. Min, M. Mao, H. Liu, G. Tu, H. Zhang, Further studies on geometric conservation law and applications to high-order finite difference schemes with stationary grids, J. Comput. Phys. 239 (2013) 90–111.

[14] X. Deng, H. Zhang, Developing high-order weighted compact nonlinear schemes, J. Comput. Phys. 165 (2000) 22–44.

[15] M.O. Domingues, S.M. Gomes, O. Roussel, K. Schneider, An adaptive multiresolution scheme with local time stepping for evolutionary PDEs, J. Comput. Phys. 227 (2008) 3758–3780.

[16] L. Han, X. Hu, N.A. Adams, Adaptive multi-resolution method for compressible multi-phase flows with sharp interface model and pyramid data structure, J. Comput. Phys. 262 (2014) 131–152.

[17] A. Harten, Adaptive multiresolution schemes for shock computations, J. Comput. Phys. 115 (1994) 319–338.

[18] A. Harten, Multiresolution algorithms for the numerical solution of hyperbolic conservation laws, Commun. Pure Appl. Math. 48 (1995) 1305–1342.

[19] G.-S. Jiang, C.-W. Shu, Efficient implementation of weighted ENO schemes, J. Comput. Phys. 126 (1996) 202–228.

[20] G.-S. Jiang, C.-C. Wu, A high-order WENO finite difference scheme for the equations of ideal magnetohydrodynamics, J. Comput. Phys. 150 (1999) 561–594.

[21] Y. Jiang, C.-W. Shu, M. Zhang, An alternative formulation of finite difference weighted ENO schemes with Lax–Wendroff time discretization for conservation laws, SIAM J. Sci. Comput. 35 (2013) A1137–A1160.

[22] Y. Jiang, C.-W. Shu, M. Zhang, Free-stream preserving finite difference schemes on curvilinear meshes, Methods Appl. Anal. 21 (2014) 1–30.

[23] J. Kok, A high-order low-dispersion symmetry-preserving finite-volume method for compressible flow on curvilinear grids, J. Comput. Phys. 228 (2009) 6811–6832.

[24] S. Komurasaki, K. Kuwahara, Implicit large eddy simulation of a subsonic flow around NACA0012 airfoil, in: 42nd AIAA Aerospace Sciences Meeting and Exhibit, 2004, p. 594.

[25] P.D. Lax, X.-D. Liu, Solution of two-dimensional Riemann problems of gas dynamics by positive schemes, SIAM J. Sci. Comput. 19 (1998) 319–340.

[26] S.K. Lele, Compact finite difference schemes with spectral-like resolution, J. Comput. Phys. 103 (1992) 16–42.

[27] X. Liu, N.R. Morgan, E.J. Lieberman, D.E. Burton, A fourth-order Lagrangian discontinuous Galerkin method using a hierarchical orthogonal basis on curvilinear grids, J. Comput. Appl. Math. 404 (2022) 113890.

[28] X.-D. Liu, S. Osher, T. Chan, Weighted essentially non-oscillatory schemes, J. Comput. Phys. 115 (1994) 200–212.

[29] P. McCorquodale, P. Ullrich, H. Johansen, P. Colella, An adaptive multiblock high-order finite-volume method for solving the shallow-water equations on the sphere, Commun. Appl. Math. Comput. Sci. 10 (2015) 121–162.

[30] G. Mengaldo, D. De Grazia, P.E. Vincent, S.J. Sherwin, On the connections between discontinuous Galerkin and flux reconstruction schemes: extension to curvilinear meshes, J. Sci. Comput. 67 (2016) 1272–1292.

[31] T. Nonomura, N. Iizuka, K. Fujii, Freestream and vortex preservation properties of high-order WENO and WCNS on curvilinear grids, Comput. Fluids 39 (2010) 197–214.

[32] T. Nonomura, D. Terakado, Y. Abe, K. Fujii, A new technique for freestream preservation of finite-difference WENO on curvilinear grid, Comput. Fluids 107 (2015) 242–255.

[33] M. Pandolfi, D. D'Ambrosio, Numerical instabilities in upwind methods: analysis and cures for the "carbuncle" phenomenon, J. Comput. Phys. 166 (2001) 271–301.

[34] J. Qiu, C.-W. Shu, Hermite WENO schemes and their application as limiters for Runge–Kutta discontinuous Galerkin method: one-dimensional case, J. Comput. Phys. 193 (2004) 115–135.

[35] O. Roussel, K. Schneider, A. Tsigulin, H. Bockhorn, A conservative fully adaptive multiresolution algorithm for parabolic PDEs, J. Comput. Phys. 188 (2003) 493–523.

[36] C.W. Schulz-Rinne, J.P. Collins, H.M. Glaz, Numerical solution of the Riemann problem for two-dimensional gas dynamics, SIAM J. Sci. Comput. 14 (1993) 1394–1414.

[37] C.-W. Shu, Essentially non-oscillatory and weighted essentially non-oscillatory schemes for hyperbolic conservation laws, in: Advanced Numerical Approximation of Nonlinear Hyperbolic Equations, Springer, 1998, pp. 325–432.

[38] H. Tang, T. Liu, A note on the conservative schemes for the Euler equations, J. Comput. Phys. 218 (2006) 451–459.

[39] M. Vinokur, H. Yee, Extension of efficient low dissipation high order schemes for 3-D curvilinear moving grids, in: Frontiers of Computational Fluid Dynamics 2002, World Scientific, 2002, pp. 129–164.

[40] M.R. Visbal, D.V. Gaitonde, On the use of higher-order finite-difference schemes on curvilinear and deforming meshes, J. Comput. Phys. 181 (2002) 155–185.

[41] P. Woodward, P. Colella, The numerical simulation of two-dimensional fluid flow with strong shocks, J. Comput. Phys. 54 (1984) 115–173.

[42] D. Xu, X. Deng, Y. Chen, Y. Dong, G. Wang, On the freestream preservation of finite volume method in curvilinear coordinates, Comput. Fluids 129 (2016) 20–32.

[43] J. Zhu, J. Qiu, A new fifth order finite difference WENO scheme for solving hyperbolic conservation laws, J. Comput. Phys. 318 (2016) 110–121.

[44] J. Zhu, J. Qiu, A new type of finite volume WENO schemes for hyperbolic conservation laws, J. Sci. Comput. 73 (2017) 1338–1359.

[45] Y. Zhu, X. Hu, Free-stream preserving linear-upwind and WENO schemes on curvilinear grids, J. Comput. Phys. 399 (2019) 108907.